PLOS Computational Biology

RESEARCH ARTICLE

Quantifying the spatiotemporal mechanical dynamics of engineered cardiac microbundles

Hiba Kobeissi[1,2], **Samuel J. DePalma**[3], **Javiera Jilberto**[3], **David Nordsletten**[3,4], **Brendon M. Baker**[3], **Emma Lejeune**[1,2]*

1 Department of Mechanical Engineering, Boston University, Boston, Massachusetts, United States of America, **2** Center for Multiscale and Translational Mechanobiology, Boston University, Boston, Massachusetts, United States of America, **3** Department of Biomedical Engineering, University of Michigan, Ann Arbor, Michigan, United States of America, **4** Department of Cardiac Surgery, University of Michigan, Ann Arbor, Michigan, United States of America

* elejeune@bu.edu

Check for updates

OPEN ACCESS

Citation: Kobeissi H, DePalma SJ, Jilberto J, Nordsletten D, Baker BM, Lejeune E (2026) Quantifying the spatiotemporal mechanical dynamics of engineered cardiac microbundles. PLoS Comput Biol 22(7): e1014522. https://doi.org/10.1371/journal.pcbi.1014522

Editor: Anna Grosberg, UCI BME: University of California Irvine Department of Biomedical Engineering, UNITED STATES OF AMERICA

Received: April 8, 2026

Accepted: July 1, 2026

Published: July 20, 2026

Peer Review History: PLOS recognizes the benefits of transparency in the peer review process; therefore, we enable the publication of all of the content of peer review and author responses alongside final, published articles. The editorial history of this article is available here: https://doi.org/10.1371/journal.pcbi.1014522

Copyright: © 2026 Kobeissi et al. This is an open access article distributed under the terms of the Creative Commons Attribution License, which permits unrestricted use, distribution,

Abstract

Brightfield time-lapse imaging is widely used in cardiac tissue engineering, yet the absence of standardized, interpretable analytical frameworks limits reproducibility and cross-platform comparison. We present an open, scalable computational pipeline for quantifying spatiotemporal contractile dynamics in microscopy videos of human induced pluripotent stem cell-derived cardiac microbundles. Building on our open-source tools "MicroBundleCompute" and "MicroBundlePillarTrack," we define a suite of 16 interpretable structural, functional, and spatiotemporal metrics that capture tissue deformation, synchrony, and heterogeneity. The framework integrates full-field displacement tracking, strain reconstruction, spatial registration, dimensionality reduction, and topology-based vector-field analysis within a unified workflow. Applied to a dataset of 670 cardiac microbundles spanning 20 experimental conditions, the pipeline reveals continuous variation in contractile phenotypes rather than discrete condition-specific clustering, with intra-condition variability often exceeding inter-condition differences. Redundancy analysis identifies a reduced core set of 10 metrics that retain most informational content while minimizing multicollinearity. Analysis of denoised displacement fields shows that contraction is dominated by a global isotropic mode, with localized saddle-type deformation patterns present in approximately half of the samples. All software and workflows are released openly to enable reproducible, scalable analysis of dynamic tissue mechanics.

Author summary

Stem cells can be guided to form many types of cells, including cardiomyocytes, offering new ways to repair damaged tissue and to model disease. In cardiac tissue engineering, human induced pluripotent stem cell-derived cardiomyocytes

and reproduction in any medium, provided the original author and source are credited.

Data availability statement: All code for extracting these direct metrics from our software tools, together with the complete post-processing workflow, is openly available on GitHub: https://github.com/HibaKob/MicroBundleAnalysis. All data is available on Dryad https://datadryad.org/dataset/doi:10.5061/dryad.3r2280gqd.

Funding: This work was supported by the CELL-MET Engineering Research Center (NSF ERC EEC-1647837 to E.L., B.M.B., and D.N.) and the National Science Foundation (Grant CMMI-2311640 to E.L.). The funders had no role in study design, data collection and analysis, decision to publish, or preparation of the manuscript.

Competing interests: The authors have declared that no competing interests exist.

(hiPSC-CMs) are grown in two- and three-dimensional systems to create functional heart tissues. These constructs, currently valuable for drug testing and heart disease modeling, are promising as future implantable patches. However, the field lacks consistent protocols and quantitative metrics that are both standardized and reproducible to evaluate tissue function. We address this need by building on our open-source tools, "MicroBundleCompute" and "MicroBundlePillarTrack," and a public dataset of videos of beating engineered tissues. We introduce quantitative metrics that describe tissue behavior across space and time, including motion patterns, beat timing, and the coordination and propagation of contraction. Using these metrics, we apply statistical analyses and machine learning approaches to identify distinct contraction phenotypes and to compare performance across samples. We also demonstrate how the choice of metrics has the potential to influence scientific conclusions. All code, documentation, and analysis workflows are openly available. By sharing these methods and a reproducible computational pipeline, we aim to support transparent benchmarking, improve cross-lab comparisons, and accelerate the development of reliable cardiac tissue models.

Introduction

Tissue engineering increasingly serves as an experimental platform for studying human tissue function by enabling the controlled fabrication of three-dimensional constructs with tunable structural and mechanical properties [1,2]. Advances in stem cell technologies [3,4], biomaterials [5,6], and microfabrication [7,8] have pushed this capability further, yielding engineered tissues of increasing complexity that more closely recapitulate native architecture and function [3–8]. In parallel, improvements in live-cell imaging and integrated culture platforms have facilitated longitudinal monitoring of these constructs, yielding rich, time-resolved datasets that capture tissue-level dynamics such as contraction, remodeling, or failure [9,10]. As a result, the overall *scale* of tissue engineering research has increased substantially, and high-throughput platforms now routinely generate large imaging datasets across many samples and conditions [11–14].

Despite this growth, quantitative methods capable of fully leveraging these data remain limited [15]. In contrast to transcriptomics, where standardized analytical frameworks and metrics have rapidly matured to support large-scale, reproducible analysis [16,17], methods for extracting and interpreting spatiotemporal mechanical information from engineered tissue datasets are still emerging. This gap is particularly acute in cardiac tissue engineering, a technically demanding domain where analysis remains highly fragmented [13,14]. Specifically, most studies rely on custom scripts and laboratory-specific workflows, limiting reproducibility, cross-study comparison, and the establishment of shared benchmarks [6,8,13,14,18]. Recent advances, including shared differentiation protocols [3,4], emerging data and metadata standards [19], publicly available datasets [20–23], and accessible analysis tools [24–38],

have begun to address these challenges. However, unified, scalable analytical workflows and standardized, interpretable metrics for heterogeneous tissue dynamics remain largely absent.

Addressing this gap requires overcoming two key challenges: (1) the absence of standardized, openly accessible computational tools for extracting quantitative information from imaging data, and (2) the lack of interpretable metrics capable of capturing spatiotemporally resolved mechanical and functional tissue behavior. Ideally, such tools would enable reproducible metric computation, while the resulting metrics would support both robust cross-sample comparison and meaningful biological interpretation. To address the first gap, we have previously developed and openly released a comprehensive computational pipeline for analyzing brightfield microscopy videos of human induced pluripotent stem cell derived cardiac microbundles (Fig 1). Specifically, our open-source tools, "MicroBundleCompute" [24] and "MicroBundlePillarTrack" [25], enable the robust extraction of full-field tissue displacement and contractile force measurements, respectively.

In this paper, we focus on the second gap and build on these tools to define a validated suite of 16 interpretable structural, functional, and spatiotemporal metrics. We showcase these metrics by applying them to a previously published dataset of 808 cardiac tissues generated using the fibroTUG platform [20,39] (Fig 1). Using integrated statistical and machine learning based analyses, we evaluate metric informativeness and redundancy, and compare the efficacy of different metrics at assessing tissue contractile behavior. All software, analysis scripts, and implementation details are openly available to support transparency, reproducibility, and ultimately broad adoption of this approach (https://github.com/HibaKob/MicroBundleAnalysis).

The remainder of this paper is organized as follows. In the "Materials and methods" Section, we detail our methodology for extracting contractile dynamics and computing interpretable metrics from microscopy videos of cardiac microbundles.

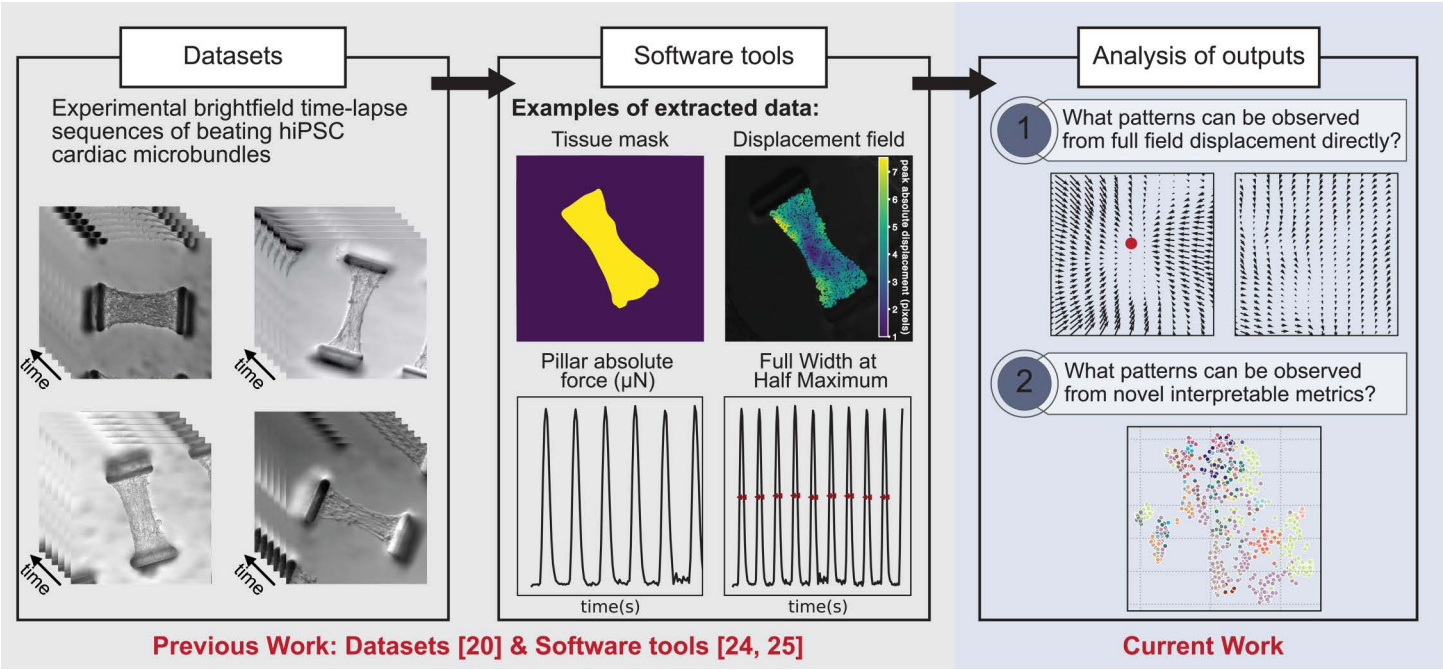


Fig 1. Overview of the study scope for mechanical analysis of engineered cardiac microbundle microscopy data. Previous work established a dataset of 808 brightfield time-lapse image sequences of contracting hiPSC-based cardiac microbundles on fibroTUG platforms [20] and open-source tools [24,25] for high-throughput extraction of tissue masks, displacement fields, and temporal contractility measures. The present work extends these efforts through analysis of the extracted outputs by (1) examining patterns in full-field displacement data and (2) defining interpretable metrics to characterize tissue behavior and dataset-level organization.

https://doi.org/10.1371/journal.pcbi.1014522.g001

We begin by introducing the experimental dataset, then describe how we use custom software to extract full-field tissue displacement and pillar force measurements. We also outline post-processing steps to address sample variability, calculate strain fields, and reduce the dimensionality of displacement data. We then present a diverse suite of structural, functional, and spatiotemporal metrics that capture the heterogeneity of tissue contractions. In the "Results and discussion" Section, we present a systematic assessment of these metrics, leverage machine learning methods to quantify informational overlap, and demonstrate how the choice of metrics influences statistical outcomes. Finally, in the "Conclusion" Section, we discuss the advances enabled by our pipeline, its strengths and limitations, and new opportunities for the field. Through this work, we establish a broadly applicable computational framework that advances interpretable metric extraction in cardiac tissue engineering, laying a foundation for rigorous quantitative analysis and meaningful biological interpretation.

Materials and methods

In this section, we present our methodology for computing the set of 16 interpretable metrics that capture the complex and heterogeneous spatiotemporal behavior of cardiac microbundles. We first introduce the experimental dataset of cardiac microbundles ("Dataset" Section), followed by a description of custom software tools used to extract displacement fields and quantify pillar forces from the recorded movies ("Time-lapse image data extraction" Section). We further describe post-processing procedures that address geometric variability across samples, compute strain fields, perform dimensionality reduction on the displacement vector fields, and analyze the resulting low-dimensional representations to identify characteristic flow and deformation patterns. Building on these data, we introduce a suite of structural, functional, and spatiotemporal metrics ("Interpretable metrics" Section), enabling a comprehensive and interpretable assessment of microbundle contractility. Although the approaches described here are demonstrated using the cardiac microbundle dataset, these methods are broadly applicable to other time-lapse image-based datasets.

Dataset

Access to openly available datasets is essential for reproducible analysis, benchmarking, and cumulative progress, particularly as tissue engineering studies generate increasingly large and complex imaging data. Consistent with open science and FAIR (Findable, Accessible, Interoperable, Reusable) principles [40,41], biomedical image analysis, including applications in tissue engineering, is increasingly adopting community-driven standards for data and metadata deposition and public release, strengthening the foundations for transparent and reproducible quantitative research [19,42–45]. Within this framework, we leverage our recently published open-access dataset to evaluate the performance and relevance of our metrics.

Specifically, we use our previously published dataset of cardiac microbundle time-lapse movies (10.5061/dryad.3r2280gqd) [20] (see Fig 2a for representative image examples). This dataset has been described in detail in previous studies [24,25,39] and comprises a total of 808 time-lapse images capturing the dynamic contractions of human induced pluripotent stem cell-derived cardiomyocyte (hiPSC-CM) microbundles on fibroTUG platforms.

FibroTUG platforms are constructed from arrays of electrospun dextran vinyl sulfone (DVS) fiber matrices [46], which are suspended between pairs of poly(dimethylsiloxane) (PDMS) cantilevers. The matrices are first functionalized with cell adhesive cyclic RGD (cRGD) peptides and subsequently seeded with differentiated and purified hiPSC-CMs [47]. Following a culture period of $3-21$ days, spontaneous microbundle contractions are recorded as time-lapse images at approximately 65 Hz using a Zeiss LSM800 equipped with an Axiocam 503 camera, at a resolution of 0.908 μm/pixel, under controlled conditions of $37^{\circ}C$ and 5% CO_2.

A key feature of the fibroTUG platforms is their versatility: (1) the mechanical stiffness of both the fiber matrix and the PDMS cantilevers can be precisely tuned by modifying the photoinitiator concentration during matrix crosslinking and adjusting the cantilever height, respectively; and (2) the alignment of the matrices can be controlled by the translation

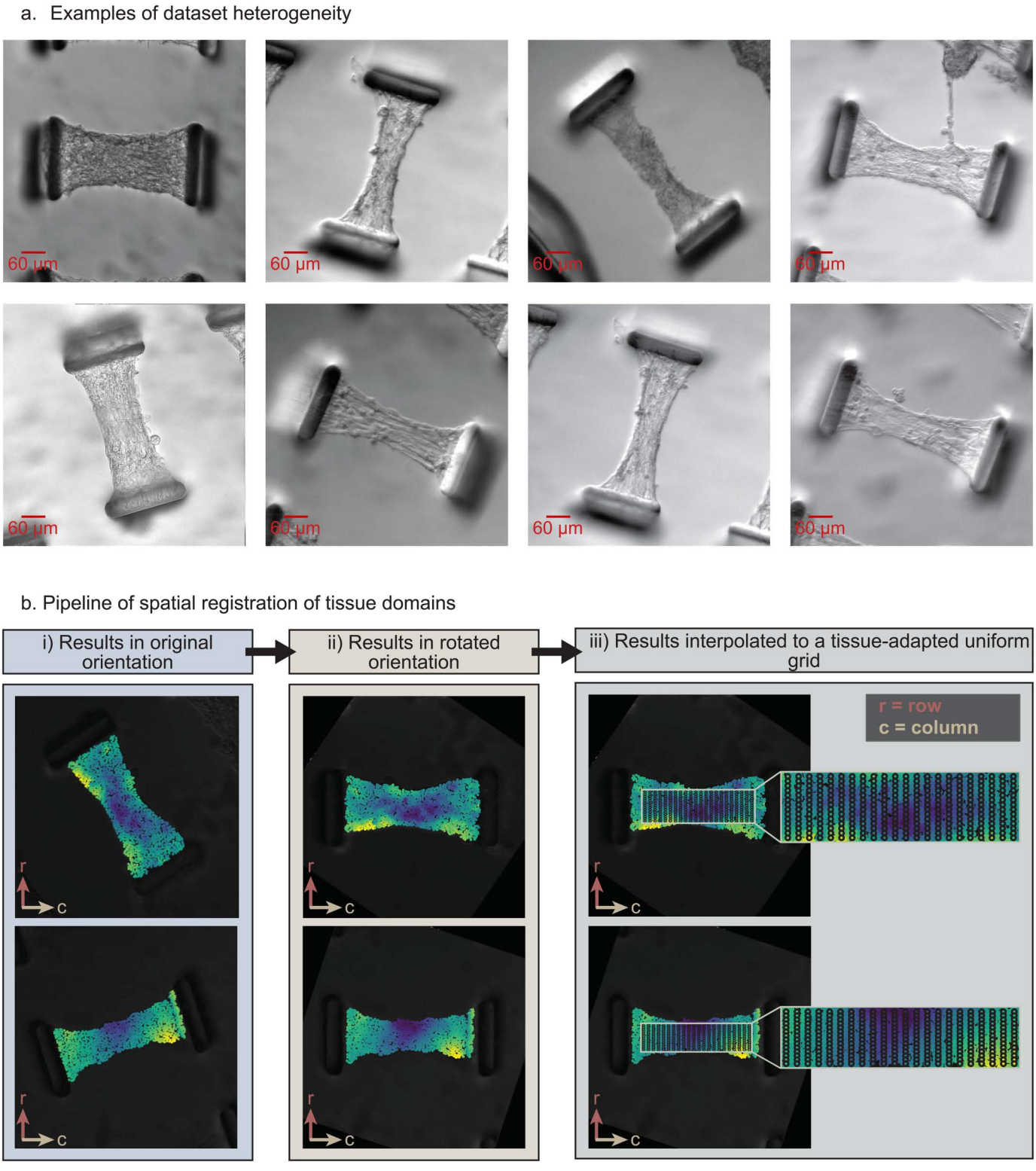


Fig 2. Spatial manipulation to standardize tissue-domain data. (a) Representative raw images from the dataset illustrating spatial heterogeneity in tissue orientation, placement, and local geometry, which complicates direct comparison across samples. **(b)** Workflow for spatial registration of tissue domains, using the absolute displacement field tracked at the identified fiducial marker points as an illustrative example: (i) per-sample results in the

original image orientation; (ii) domains rotated to a common axis to homogenize orientation across the dataset; (iii) rotated domains interpolated onto a tissue-adapted uniform grid to produce consistently sampled measurements along the tissue axis (inset: zoomed-in view showing both the original fiducial marker distribution and the uniform interpolation grid). This two-step manipulation, consisting of rotation followed by interpolation, preserves local spatial features while enabling direct pixel-wise comparisons and downstream analyses.

https://doi.org/10.1371/journal.pcbi.1014522.g002

speed of the mandrel during fiber deposition. By systematically varying these parameters, the dataset encompasses a broad range of biomechanical and structural environments across 20 distinct experimental conditions.

Further details on experimental protocols, matrix fabrication, and metadata can be found in the published dataset and accompanying resources [20,24,25,39,46,47]. Though this manuscript presents results on the fibroTUG microscopy movies exclusively, the methods presented here are extensible to all time-lapse images of cardiac tissue across different experimental platforms and imaging modalities where approximating full-field deformation is feasible [31,48–51].

Time-lapse image data extraction

For the dataset described in the "Dataset" Section, we first performed detailed analysis of the microscopy movies using our previously developed tracking and quantification software, "MicroBundlePillarTrack" [25] and "MicroBundleCompute" [24]. Out of the initial 808 samples, 670 were processed successfully. Specifically, the software failed on 100 examples due to data quality issues, as detailed in the "Software failure and data exclusion" Section. Additional 38 examples were excluded from further analysis due to structural issues with the tissue, such as being excessively thin, having extensions that extended beyond the width of the pillars causing unbalanced mechanical behavior, or showing partial detachment from one of the anchoring pillars.

As described in the "Dataset" Section, the present work focuses on the fibroTUG dataset of cardiac microtissues. These tissues are not conventional 2D monolayers, but instead consist of electrospun fiber matrices suspended between flexible posts, and are therefore more appropriately considered quasi-3D or 2.5D engineered tissues. More broadly, the proposed framework is applicable to time-lapse images of engineered cardiac tissues acquired across different experimental platforms, provided that tissue motion can be approximated from the available image data. As a demonstration of this broader applicability, in previous work we implemented and extensively validated both "MicroBundlePillarTrack" [25] and "MicroBundleCompute" [24] on standard 3D cardiac microbundles grown on strain gauge platforms [21].

MicroBundlePillarTrack. We developed "MicroBundlePillarTrack" [25] as a robust, open-source software tool for automated segmentation, tracking, and analysis of pillar deflection in beating microbundles imaged using brightfield microscopy. The software processes consecutive frames of a movie, automatically generating two distinct binary masks to delineate each pillar. After segmentation, fiducial markers identified using the Shi–Tomasi corner detection method [52] on the first relaxed frame, are tracked throughout all subsequent frames via a pyramidal implementation of the Lucas–Kanade sparse optical flow algorithm [53,54]. This approach enables precise determination of pillar positions across time, from which both mean directional and absolute displacements are calculated. The software further derives quantitative outputs including microbundle twitch force and stress, as well as temporal metrics such as contraction and relaxation velocities, Full Width at Half Maximum (FWHM), and Full Width at 80% maximum (FW80M), where FWHM and FW80M are defined as the temporal width of the mean absolute displacement curve at 50% and 80% of its peak amplitude, respectively (Fig 4). As measures of contraction duration, FWHM and FW80M are analogous to width-based metrics commonly computed from calcium transients to characterize the duration of calcium activation in engineered cardiac tissues [39,55,56].

Notably, "MicroBundlePillarTrack" [25] requires no parameter tuning, streamlining the high-throughput analysis of large datasets. Required user input is minimal and limited to frame rate (fps), length scale (μm/pixel), pillar stiffness (μN/μm), and tissue thickness (μm). A comprehensive description of the software's methodology and capabilities can be found in its primary publication [25].

For the present study, we primarily utilize outputs from "MicroBundlePillarTrack" [25] related to pillar force and the temporal metric Full Width at Half Maximum (derived from the pillar mean absolute displacement time series), which become interpretable metrics detailed in the "Interpretable metrics" Section.

MicroBundleCompute. Our tool "MicroBundleCompute" [24] is also an optical flow-based tracking and analysis software, and is among the few specialized tools available for whole-tissue deformation analysis in microscopy movies of cardiac microbundles [26,57,58]. "MicroBundleCompute" is specifically designed for multi-purpose assessment of heterogeneous cardiac microbundle deformation and strain from brightfield and phase contrast videos, and the software has been extensively validated to ensure robust and reliable performance.

Analogous to "MicroBundlePillarTrack" [25], "MicroBundleCompute" [24] automatically generates a binary mask of the tissue and identifies "good features to track" marker points using Shi–Tomasi corner detection [52] within the masked region on the first relaxed frame. These points are then tracked across all frames, employing a sparse optical flow [53,54] approach and segmenting the analysis by individual contraction cycles to mitigate noise accumulation associated with extended temporal tracking. This process yields high-resolution vector maps of tissue displacements throughout the contraction-relaxation cycle, as the tracking code automatically ensures sufficient density and spatial coverage of fiducial markers across the tissue domain, with a minimum of one fiducial marker enforced for every subdivision of 50 pixels of tissue area (see Figs 2b and S1 Fig for representative examples of fiducial marker density and distribution). These vector maps further facilitate the calculation of spatially-averaged Green-Lagrange strain within specified tissue subdomains. Post-processing modules further enhance analytical rigor by allowing for automated rotational alignment of image stacks and tracked data, as well as interpolation of displacement and strain fields onto query grids for spatiotemporal analyses. Importantly, the software is optimized for batch processing and requires minimal user intervention, with only the frame rate (fps) and pixel-to-micrometer conversion factor specified by the user. All other parameters are internally standardized to maintain analytic consistency across large datasets. For an in-depth description of the software's methods and functionalities, as well as further details on its implementation and usage, please refer to the original publication [24].

In the present study, we utilize the two-dimensional displacement fields generated by "MicroBundleCompute" [24] for direct computation of full-field Green-Lagrange strain, as outlined in the "Strain computation details" Section. These computational outputs serve as the starting point for a substantial subset of the interpretable metrics described in the "Interpretable metrics" Section, supporting rigorous, spatially resolved characterization of contractile tissue mechanics.

Strain computation details. As described in the "MicroBundleCompute" Section, "MicroBundleCompute" [24] is specifically designed to calculate average subdomain strain rather than full-field strain. In this approach, the displacements of all fiducial markers within each subdomain are used to approximate an averaged deformation, from which a single representative strain value is derived rather than a spatially resolved estimate at each marker location. This design choice was motivated by two main considerations: (1) minimizing the impact of imaging artifacts and noise, and (2) facilitating more consistent comparisons across different samples. While the subdomain averaging approach is practical and robust, it inherently restricts the spatial resolution of strain quantification, since the strain in each subdomain is estimated from the available fiducial marker points and requires a minimum number of points to ensure mathematical stability, particularly to avoid singular matrices during computations.

For our current study, we sought higher spatial resolution in strain mapping than what the subdomain-based method can provide. To achieve this, we adopted the approach described by Zimmerman et al. [59] and Benkley et al. [60], which enables computation of a two-dimensional Green-Lagrange strain field. This method estimates the local deformation gradient tensor directly from the tracked positions of randomly distributed particles, utilizing a least-squares fitting procedure on nearest-neighbor vectors combined with a first-order finite difference approximation (S1 Fig). In mathematical terms, the estimated deformation gradient **F** at a given point α can be expressed as follows [59]:

$$\mathbf{F}^{\alpha} = \left[\sum_{\beta=1}^{n} \mathbf{x}^{\alpha\beta} \left(\mathbf{X}^{\alpha\beta}\right)^{\top}\right] \left[\sum_{\beta=1}^{n} \mathbf{X}^{\alpha\beta} \left(\mathbf{X}^{\alpha\beta}\right)^{\top}\right]^{-1} \tag{1}$$

where $\mathbf{x}^{\alpha\beta}$ represents the vector connecting marker points α and β in the current (deformed) configuration, while $\mathbf{X}^{\alpha\beta}$ denotes the corresponding vector in the reference (undeformed) configuration. The parameter *n* specifies the total number of non-collinear neighboring marker points used in the estimation, which, for our analysis, was set to 8 to ensure robust and accurate computation of the local deformation gradient.

Computing the Green-Lagrange strain (**E**) tensor from the deformation gradient tensor is straightforward:

$$\mathbf{E}^{\alpha} = \frac{1}{2}\left[(\mathbf{F}^{\alpha})^{\top}\mathbf{F}^{\alpha} - \mathbf{I}\right] \tag{2}$$

where **I** is a 2×2 identity matrix.

We provide our Python implementation of this strain computation approach, enabling users to derive strain fields from displacement data obtained via "MicroBundleCompute" [24]. This code, along with all of the scripts used to calculate the defined metrics in the "Interpretable metrics" Section, are made available on GitHub (https://github.com/HibaKob/MicroBundleAnalysis) to allow others to reproduce and build on our methods.

Software failure and data exclusion. The failure of 100 microscopy movies to be processed successfully can be attributed to specific design requirements and stringent algorithmic constraints within "MicroBundleCompute" [24] and "MicroBundlePillarTrack" [25]. Specifically, two principal categories of movies were excluded: (1) those with blurred frames, which compromise image quality and hinder the accurate identification of fiducial markers essential for robust tracking; and (2) those comprising fewer than three contraction beats, which provide insufficient temporal information for meaningful characterization of contractile dynamics. By enforcing these exclusion criteria, the software ensures that only movies capable of yielding precise and interpretable results are included in subsequent analysis.

Spatial registration of tissue domains. The images present in this dataset are taken at multiple different angles, and individual tissues vary in size (Fig 2a). To make direct comparisons between these tissues, we began by performing a systematic registration of tissue domains using masks automatically generated by MicroBundleCompute (Fig 2b) [24]. Each mask was rotated so that the tissue's major axis aligns with the horizontal (column) axis, and a mean tissue mask was then computed from the set of aligned and rotated masks. To ensure standardized subsequent analyses, we performed a grid sensitivity analysis (S2 Fig) on the metrics defined in the "Interpretable metrics" Section, which informed the selection of a regular grid with a resolution of 28×33, centered on the mean mask and spanning 80% of its width and height. For each individual tissue, we calculated an affine transformation that maps the example rotated tissue mask onto the mean tissue mask. This transformation was then used to register the reference grid onto the individual tissue, thereby defining a tissue-specific grid. To enable direct comparisons across tissues, the field of interest (either displacement or strain) was interpolated onto each tissue-specific grid using SciPy's Radial Basis Function (RBF) interpolation (v1.13.1) [61,62]. This workflow is critical for ensuring robust and spatially consistent comparisons across heterogeneous microbundle time-lapse images, enabling meaningful downstream analyses that would otherwise be confounded by variations in tissue orientation, size, and geometry.

It is worth noting that variability in tissue orientation and geometry is an inherent challenge across engineered heart tissue datasets, irrespective of experimental platform. The registration and grid optimization workflow detailed above is therefore not dataset-specific; rather, it is designed to be broadly applicable to alternative tissue geometries and experimental configurations. For datasets derived from distinct microbundle architectures or fabrication platforms, the grid sensitivity analysis outlined in this section would need to be repeated to identify a resolution that adequately captures

spatially heterogeneous contractile behavior. The affine registration framework and RBF interpolation pipeline are similarly generalizable, provided that reliable tissue masks can be automatically or semi-automatically generated. Collectively, the methodology presented here establishes a systematic and extensible protocol for spatially consistent cross-tissue comparisons, accommodating the geometric diversity inherent to engineered cardiac tissue datasets produced across different experimental systems.

Principal component analysis

Principal component analysis (PCA) [63,64] is a widely used unsupervised multivariate analysis technique that transforms complex datasets by projecting them onto a lower-dimensional orthogonal subspace. Typically, the number of retained principal components is far fewer than the original dimensions of the data, resulting in a more concise and informative representation. When applied to vector fields, PCA identifies the primary directions of variation, enabling significant reduction in dimensionality while efficiently filtering out noise and redundancy [65–68]. Moreover, the dominant principal components not only capture the most meaningful patterns within the data, but also provide valuable physical insight into the underlying deformation modes and structures of the system under study [65,67,68].

In this study, PCA was applied to the displacement vector fields within the beating cardiac microbundles, as extracted by "MicroBundleCompute" [24]. Our primary motivation for implementing principal component analysis in this study is twofold. First, we seek to uncover latent patterns within the displacement vector field that may reveal meaningful insights into the contractile behavior of cardiac microbundles. Second, we use PCA in this context to denoise the displacement data to enable additional analysis. By reconstructing each tissue's displacement vector field using only the first 10 principal components, which capture approximately 93% of the total variance, we effectively remove noise and redundancy, producing cleaner datasets that are better suited for future metric extraction and quantitative analysis.

Given the inherent complexity and spatiotemporal variability of the raw displacement data across samples, two preprocessing steps are required to achieve both objectives. First, we performed temporal homogenization by selecting the displacement field at a single time point corresponding to peak tissue contraction. Next, as detailed in the "Spatial registration of tissue domains" Section, we spatially homogenized the dataset by interpolating the displacement fields of all 670 cardiac microbundle samples onto a unified 28×33 grid. This careful standardization of both temporal and spatial dimensions ensures consistency across examples.

To organize the data for PCA, we first retained the spatial structure of the grid points and constructed two three-dimensional matrices of size $28 \times 33 \times 670$: one for the horizontal (column) and one for the vertical (row) components of the displacement field. In each matrix, the first two dimensions represent the row and column positions on the spatial grid, while the third dimension indexes the 670 tissue samples. We then transformed both 3D matrices into a 2D format suitable for PCA by performing mode-3 unfolding, as described in [69,70]. Specifically, each $28 \times 33 \times 670$ matrix was independently reshaped into a 670×924 matrix, where each row corresponds to a tissue sample and each column to a specific spatial displacement feature. We then concatenated the two unfolded matrices, corresponding to the horizontal and vertical displacement components respectively, along the feature axis, resulting in a final data matrix ($\mathbf{Q}$) of size 670×1848. This organization allows each tissue sample to be represented as a single vector of 1,848 displacement features, enabling a comprehensive and meaningful principal component analysis.

We performed PCA using the Python library scikit-learn (v1.7.1) [71] on the data matrix $\mathbf{Q}$. In accordance with the standard PCA theory, the process begins by centering the data, which involves subtracting the mean from each column to ensure that the analysis captures variance relative to the mean. The subsequent steps differ in implementation from the classical covariance-based derivation, but they yield mathematically equivalent results. Instead of explicitly forming the covariance matrix and performing an eigenvalue decomposition, scikit-learn performs a singular value decomposition (SVD) of the centered data matrix. Given a centered data matrix $\mathbf{Q_c}$, it computes $\mathbf{Q_c} = \mathbf{U}\Sigma\mathbf{V}^\top$; the principal axes (directions) are the right singular vectors $\mathbf{V}$, and the explained variances are $\Sigma^2/(n-1)$, which are mathematically equivalent to the eigenvectors and

eigenvalues of the covariance matrix $\mathbf{C} = [1/(n-1)]\mathbf{Q_c}^\top \mathbf{Q_c}$ [72]. This approach avoids explicitly constructing the covariance matrix, which improves numerical stability and is more memory- and compute-efficient for large or high-dimensional datasets. Finally, the principal component scores, or in other words, the transformed variables summarizing the dominant patterns in the data, are obtained as scores = $\mathbf{Q_cV}$, that is by projecting the centered data onto the principal axes.

Finally, we make our complete implementation of PCA publicly available on GitHub (https://github.com/HibaKob/Micro-BundleAnalysis), including detailed steps for matrix unfolding and the construction of the data matrix *Q*. We present the results of this analysis in the "Principal Component Analysis uncovers primary isotropic contraction mode in tissue displacement" Section.

Critical point analysis

Analysis of two-dimensional vector field topology has been foundational in fluid dynamics, where it is particularly useful for studying velocity fields in turbulent flows that exhibit intricate and dynamic patterns [73,74]. This approach not only facilitates intuitive visual representation of complex datasets, making them more accessible for human interpretation, but also enables the identification and classification of a broad spectrum of wave phenomena [73–76]. Central to this methodology is critical point analysis, which detects and categorizes local flow patterns and spatial features within vector fields at fixed time points, thereby enabling the identification of spatiotemporal wave phenomena through their evolution in time [75–80]. While rooted in fluid dynamics, the mathematical foundations of critical point analysis are applicable to any continuous vector field, regardless of the underlying physical phenomenon, and its versatility has captured the interest of researchers across a broad range of disciplines. This has led to the adoption and extension of these methods in diverse fields such as neural circuit analysis and brain activity pattern detection [81–83], transcriptomics and cell fate mapping [84–86], and the detection of irregularities in cardiac electrophysiology [87,88].

Building on these advances, we further extend critical point analysis to the study of dynamic cardiac tissue behavior. By applying this technique to PCA-denoised displacement vector fields reconstructed for each tissue, we aim to identify and characterize significant localized spatial patterns underlying tissue contraction and coordination.

Critical points are locations where the vector magnitude is zero, and they are classified into six main types based on the behavior of nearby tangent curves (Fig 3a), with nodes and foci each further distinguished into stable and unstable variants. These primary types include: (1) saddles, characterized by one stable and one unstable axis, often arising from interactions or collisions of different wavefronts; (2) nodes, which act as sinks (stable) or sources (unstable) and represent regions where flow contracts toward or expands from a central point; and (3) foci, around which flow spirals, corresponding to contracting (stable) or expanding (unstable) spiral waves [75,79,89,90].

In our implementation, critical point analysis was performed on the reconstructed displacement vector field for each tissue, using only the first 10 principal components (see "Principal component analysis" Section) to capture the most salient displacement patterns at peak contraction. The reconstructed field was then reshaped into horizontal and vertical displacement components on the unified 28×33 spatial grid, yielding a denoised two-dimensional displacement vector field for each tissue.

Critical points were subsequently identified and characterized in these reconstructed fields according to established methods from prior literature [78–80]. Specifically, a grid-based Poincaré Index approach was employed [91], under the assumption that the vector field varies piecewise linearly within each grid cell.

Given that our reconstructed displacement field per tissue is represented on a 28×33 grid, we partitioned the grid into an oriented triangular mesh, and each triangle was evaluated for the presence of a critical point. For each triangle, we calculated the winding number as follows [81]:

$$\text{winding number} = \frac{1}{2\pi}\sum_{k=1}^{n}\left(\theta_{k+1}-\theta_k\right), \qquad \left(\theta_{k+1}-\theta_k\right) \in \left[-\pi, \pi\right] \tag{3}$$

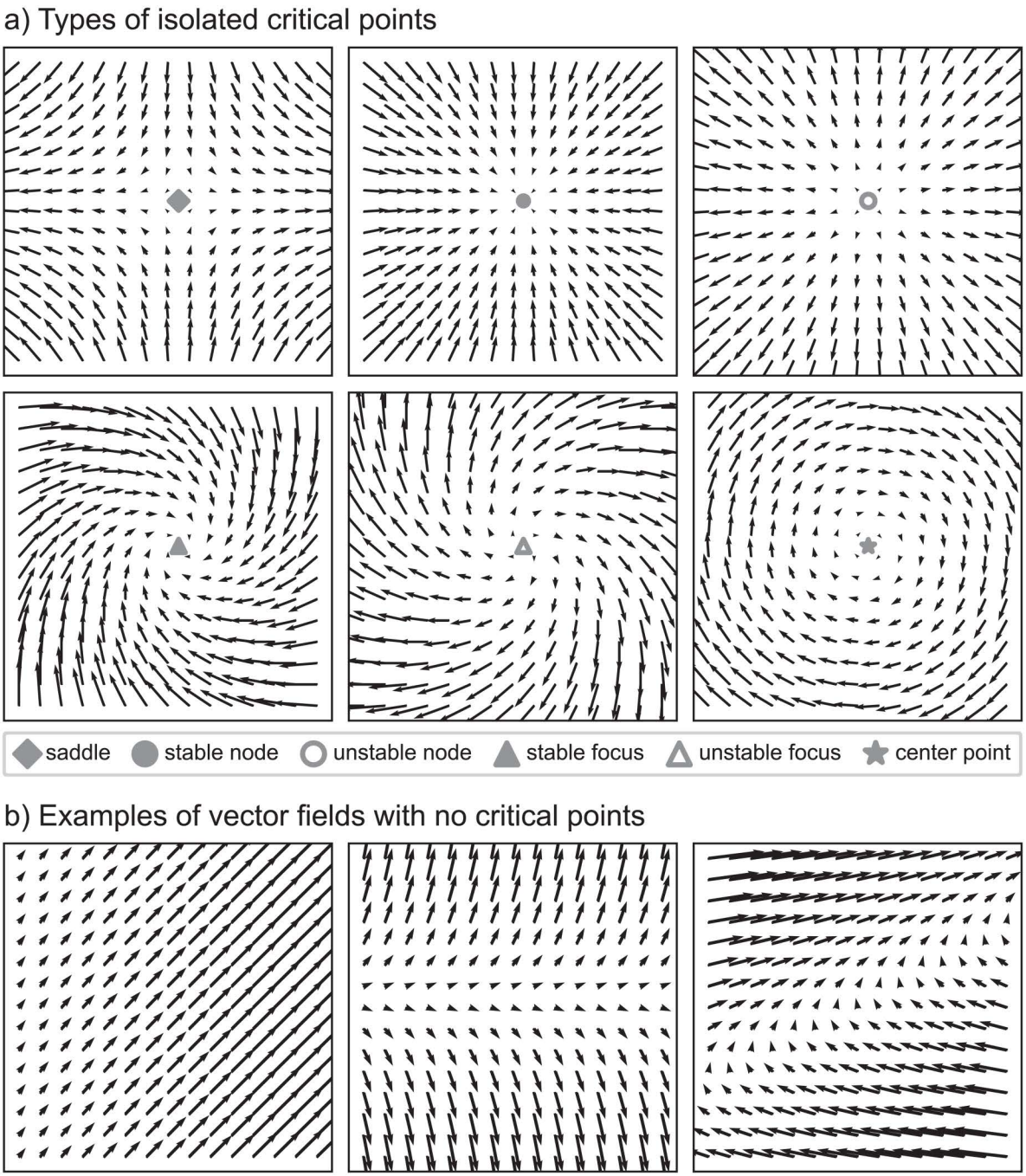


Fig 3. Illustrative 2-dimensional vector fields constructed to demonstrate the types of critical points identified through critical point analysis. (a) isolated first-order critical points; (b) examples of vector fields in which no critical points are detected, demonstrating flows without singularities.

https://doi.org/10.1371/journal.pcbi.1014522.g003

where $n = 3$ for a triangle, and θ_k denotes the angle of the displacement vector at the k^{th} vertex along the triangle boundary. Here, k indexes the ordered spatial vertices of the triangle, taken in counterclockwise order, with circular indexing such that $\theta_{n+1} = \theta_1$. The angular differences were wrapped to the interval $[-\pi, \pi]$. Based on the computed winding number for each triangle, we identified three possible scenarios:

- winding number = 1: indicates the presence of a node or focus critical point within the triangle (Fig 3a);
- winding number = -1: indicates the presence of a saddle critical point (Fig 3a);
- winding number = 0: indicates no critical point within the triangle (Fig 3b).

When a nonzero winding number is detected, we used the piecewise linear approximation of the displacement field within the element to locate the critical point, solving for the position where the vector field vanishes in both horizontal (column) and vertical (row) directions. To further characterize the nature of each critical point, we computed the Jacobian matrix **J** for the corresponding triangle, ensuring it is non-degenerate ($\det(\mathbf{J}) \neq 0$). We then solved the characteristic equation to obtain the eigenvalues:

$$\lambda \mathbf{x} = \mathbf{J}\mathbf{x}, \qquad \lambda = \mathrm{Re}_{1,2} + i\,\mathrm{Im}_{1,2} \tag{4}$$

We then classified the critical points based on the real and imaginary components of the eigenvalues:

- stable node: $\mathrm{Re}_1, \mathrm{Re}_2 < 0$, $\mathrm{Im}_1 = \mathrm{Im}_2 = 0$
- unstable node: $\mathrm{Re}_1, \mathrm{Re}_2 > 0$, $\mathrm{Im}_1 = \mathrm{Im}_2 = 0$
- stable focus: $\mathrm{Re}_1, \mathrm{Re}_2 < 0$, $\mathrm{Im}_1 \times \mathrm{Im}_2 < 0$
- unstable focus: $\mathrm{Re}_1, \mathrm{Re}_2 > 0$, $\mathrm{Im}_1 \times \mathrm{Im}_2 < 0$
- center point: $\mathrm{Re}_1 = \mathrm{Re}_2 = 0$, $\mathrm{Im}_1 \neq \mathrm{Im}_2 \neq 0$

Our complete Python implementation of this critical point analysis, including mesh generation and eigenvalue computation, is available on GitHub: https://github.com/HibaKob/MicroBundleAnalysis. In the "Critical point analysis provides complementary insights to PCA" Section, we show the corresponding findings.

Interpretable metrics

While dimensionality reduction and topological analysis reveal dominant contraction modes and localized deformation patterns, they do not yield quantitative descriptors suitable for systematic comparison across tissues. In addition, conventional workflows that compare between tissue typically lack explicit measures for quantifying asynchrony and heterogeneity in contractile behavior across the tissue domain [14].

Here, we introduce a suite of structural, functional, and spatiotemporal metrics (Fig 4a), adapted from disciplines including optimal transport [92], neural activity analysis [93], and automatic speech recognition [94], specifically tailored to quantify the heterogeneous and dynamic behavior observed in cardiac tissues.

Wasserstein distance. The Wasserstein distance, also known as Earth Mover's Distance, is a widely used metric for quantifying the difference between two probability distributions. Originally formulated by Rubner et al. [92,95], the Wasserstein distance measures the minimal "work" required to transform one distribution into another. In vector field analysis [96,97], it has been used to quantitatively compare computational and experimental flow fields under equivalent conditions, thereby providing an interpretable measure of differences between complex vector field patterns.

In this work, we use the Wasserstein distance to quantify the difference between the original displacement field at peak tissue contraction, interpolated onto a tissue-specific 28×33 grid (see "Spatial registration of tissue domains" Section), and its reconstruction from the first 10 principal components (see "Principal component analysis" Section). This approach allows us to assess the overall similarity between the two vector-valued distributions, where a larger Wasserstein distance indicates greater dissimilarity in the displacement patterns and suggests that the original field contained greater irregularities not preserved in the PCA-based reconstruction (Fig 4b-iv). By comparing the two displacement vector field distributions, the Wasserstein distance provides a measure of reconstruction fidelity beyond point-wise error metrics.

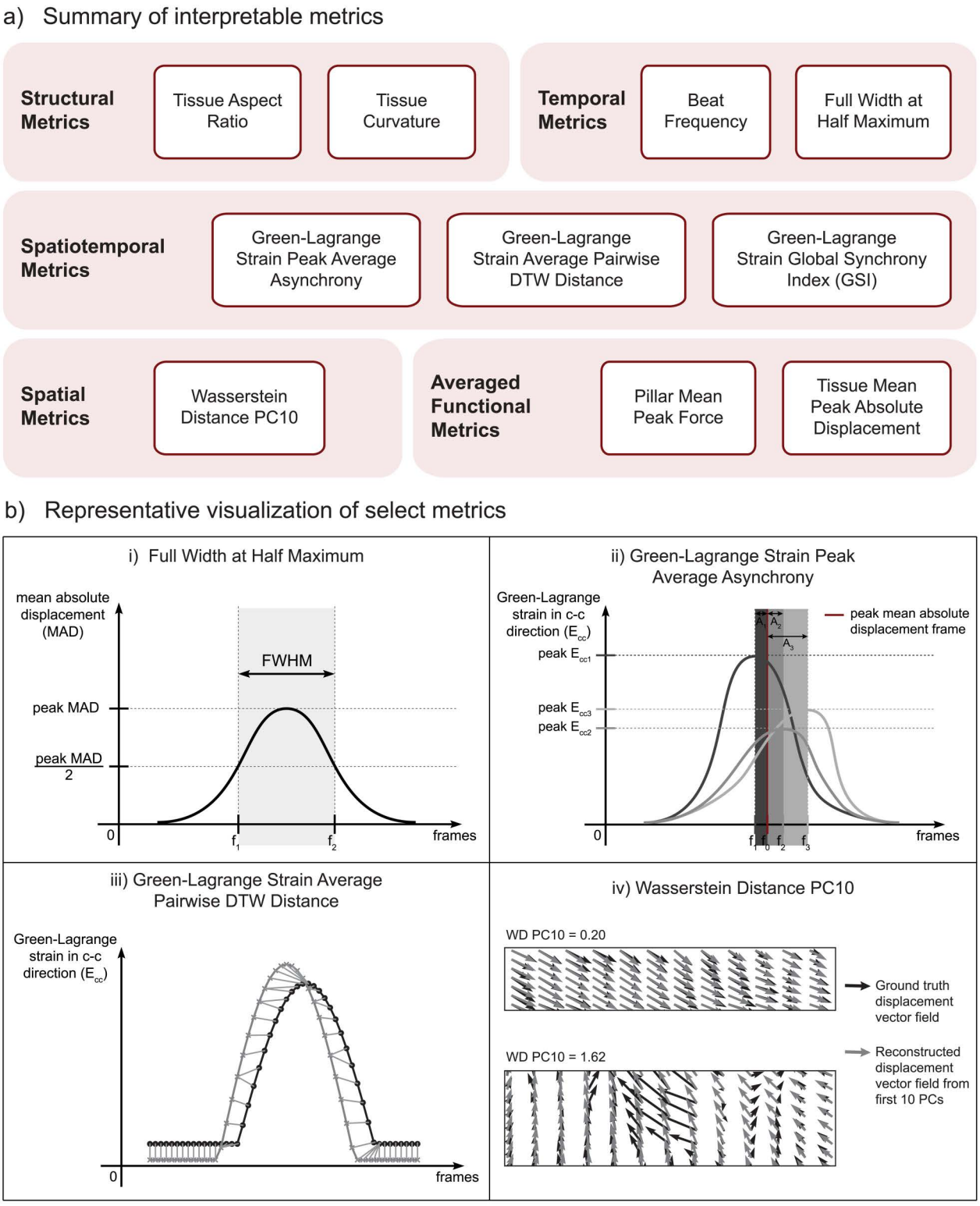


Fig 4. Summary of interpretable metrics and example computations. (a) Organized grouping of the metrics by the type of descriptive information they provide. **(b)** Representative visualizations showing how select, less-intuitive metrics are computed: **(i)** Full Width at Half Maximum (FWHM)–the

temporal width of the mean absolute displacement (MAD) curve at half its peak amplitude, obtained as $f_2 - f_1$; **(ii)** Green–Lagrange Strain Peak Average Asynchrony– $A_1 \cdots An$, the differences between the timing of peak strain across spatial locations relative to the tissue's peak mean absolute displacement are used to compute the average asynchrony; **(iii)** Green–Lagrange Strain Average Pairwise DTW Distance–example of pairwise dynamic time warping (DTW) distance between two strain time series from different locations within the tissue; **(iv)** Wasserstein Distance PC10–comparison of ground-truth and reconstructed displacement vector fields using the first 10 principal components, with shown Wasserstein distance values illustrating low (Wasserstein Distance PC10 = 0.20) versus high (Wasserstein Distance PC10 = 1.62) distance.

https://doi.org/10.1371/journal.pcbi.1014522.g004

The first Wasserstein distance between two distributions, using the Euclidean norm as the ground metric, is defined as [98]:

$$l_1(u, v) = \inf_{\pi \in \Gamma(u,v)} \int_{\mathbb{R}^n \times \mathbb{R}^n} \|x - y\|_2 \, d\pi(x, y) \tag{5}$$

where $\Gamma(u, v)$ denotes the set of distributions with marginals u and v, π is a transport plan, and $\|x - y\|_2$ is the Euclidean distance between x and y in $\mathbb{R}^n$. In the discrete setting, the Wasserstein distance can be interpreted as the cost of an optimal transport plan required to transform one distribution into the other, where the cost is given by the amount of probability mass moved multiplied by the distance over which it is transported. In this setting, the finite point sets $\{x_i\}$ and $\{y_j\}$ denote the support set of the probability mass functions u and v, respectively.

To compute the Wasserstein distance in our analysis, the `wasserstein_distance_nd` function [99,100], available in SciPy (v1.13.1) [61], was used. This function enables the efficient computation of the Wasserstein distance between N-dimensional discrete distributions. In this implementation, the inputs `u_values` and `v_values` correspond to the 2D displacement vectors from the original and reconstructed fields, respectively. The optional inputs `u_weights` and `v_weights` specify the associated nonnegative weights of the support points; however, these arguments were not provided in the present analysis, and equal weight ($1/M$) was therefore assigned to all support points, where $M = 924$ denotes the number of grid points. For transparency and reproducibility, the complete script for implementing this function, as well as the procedure for reconstructing the displacement fields, is provided on GitHub: https://github.com/HibaKob/MicroBundleAnalysis. We present the results of this analysis in the "Feature correlations reflect both redundancy and novel information" Section.

Global synchrony index (GSI). In order to quantitatively assess synchronization across multiple neuronal population time series, Li et al. [93] introduced the normalized global synchrony index (GSI). This metric provides an interpretable scale where a value of 0 denotes complete asynchrony among time series, and a value of 1 represents perfect synchrony (Fig 5, left panel). In our dataset, the GSI is well-suited for the quantification of regional synchrony within tissue samples. In particular, the Green-Lagrange strain fields, evaluated on unified grids (see "Spatial registration of tissue domains" Section), display peak strain values that do not necessarily occur at the same time frame across all grid locations.

To apply the global synchrony index to our tissue data, we computed GSI values for each tissue sample and for each of the three Green-Lagrange strain components: E_{cc} (column-column based on row-column descriptions of image data, representing the main axis of tissue contraction), E_{rr} (row-row, normal to the main contraction axis), and E_{cr} (column-row). In order to make the synchrony metric comparable across all 670 tissue examples, we homogenized the temporal profiles of the strain fields by rescaling each time series to span a normalized interval from 0 to 1 time units. For computational consistency, we sampled 25 equally spaced time points within this interval, using steps of 0.04 units. This sampling density was selected as a practical balance between preserving sufficient temporal resolution to capture waveform dynamics and avoiding unnecessary oversampling. At these standardized time points, strain values for each spatial grid location were interpolated using SciPy's (v1.13.1) [61] CubicSpline implementation. This approach ensures that the GSI reflects true differences in strain synchrony across spatial regions and tissue samples, independent of variations in tissue beating frequency.

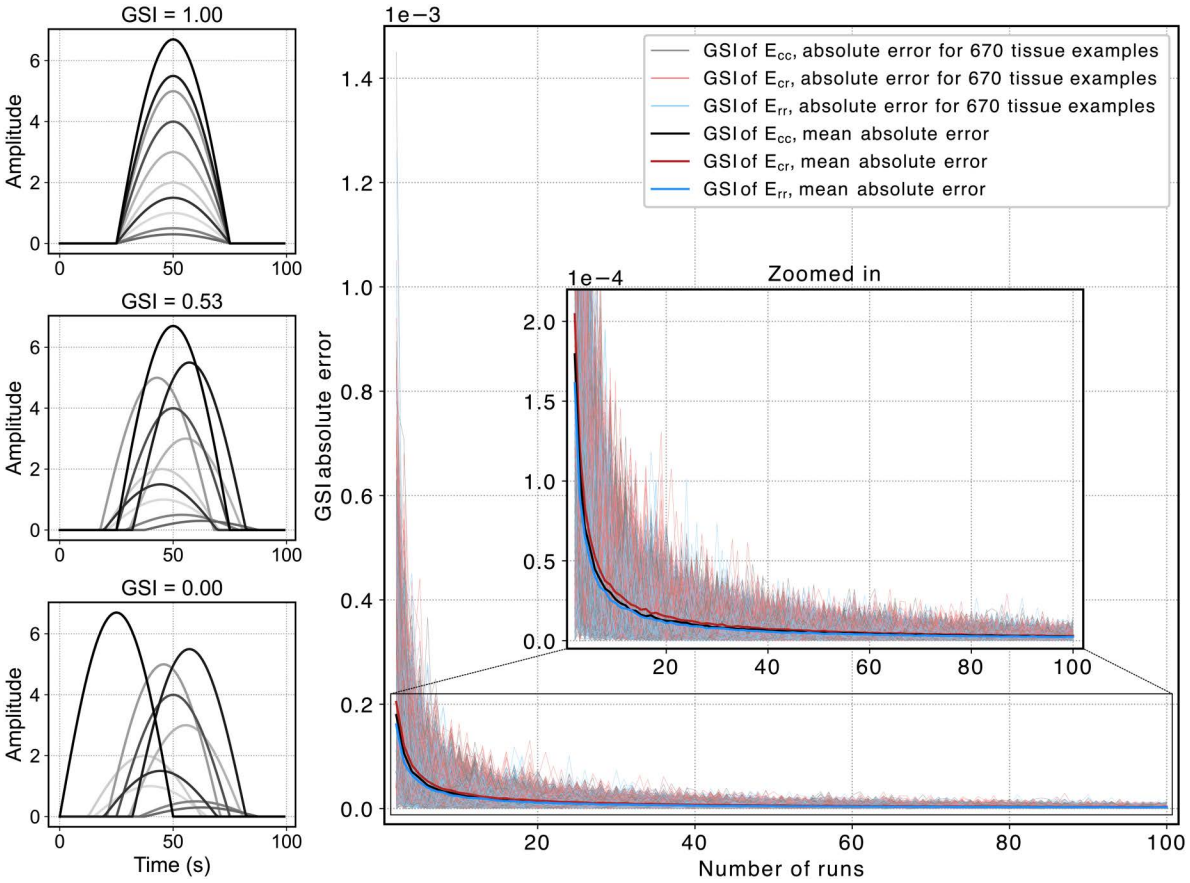


Fig 5. Convergence analysis of the normalized global synchrony index (GSI) for 670 tissue examples over 100 independent runs. The left panel presents representative strain time series for varying degrees of synchrony: perfect synchrony (GSI = 1.00), moderate synchrony (GSI = 0.53), and complete asynchrony (GSI = 0.00), exemplifying how the GSI reflects regional temporal alignment in tissue deformation. The right panel illustrates the reduction in GSI mean absolute error as a function of the number of runs, demonstrating that the mean GSI values stabilize after approximately 80 runs for all three strain components (E_{cc}, E_{cr}, and E_{rr}).

https://doi.org/10.1371/journal.pcbi.1014522.g005

The global synchrony index (GSI) was implemented following the framework established by Li et al. [93], which leverages random matrix theory and equal-time correlation matrix analysis. For each tissue sample, the temporally homogenized strain data were organized as $M = 924$ strain time series, one per spatial grid location, each sampled at $T = 25$ normalized time points. The Pearson correlation matrix $\mathbf{R} \in \mathbb{R}^{M \times M}$ was then constructed, where $R_{ij} = \text{corr}(\mathbf{x}_i, \mathbf{x}_j)$, and $\mathbf{x}_i$ and $\mathbf{x}_j$ denote the strain time series at grid locations i and j, respectively. Thus, each entry of $\mathbf{R}$ measures the equal-time temporal association between a pair of spatial locations within the tissue.

We then performed eigenvalue decomposition of $\mathbf{R}$ with the largest eigenvalue λ serving as a robust measure of global synchronization across the tissue [93,101]. To ensure that the GSI values accurately reflect true synchronization rather than statistical artifacts, we normalized λ using randomized surrogate datasets generated via amplitude-adjusted Fourier transform (AAFT). AAFT effectively preserves the amplitude distribution and approximate autocorrelation structure of each time series while removing genuine equal-time correlations. For each tissue sample, this randomization was repeated 100 times, and the maximum eigenvalue λ' was recorded for each realization. We then calculated the mean ($\bar{\lambda}'$) and the standard deviation (SD) of these surrogate eigenvalues to provide a robust estimate of expected synchronization under random conditions.

The normalized GSI value was then calculated as follows:

$$\mathrm{GSI}_{norm} = \begin{cases} \left(\lambda - \bar{\lambda}'\right) / \left(M - \bar{\lambda}'\right) & \text{if } \lambda > \bar{\lambda}' + K \times SD \\ 0 & \text{otherwise} \end{cases} \quad (6)$$

where K is the Bonferroni-adjusted critical value from the standard normal distribution to control the overall probability of a Type I error (false positive) for multiple hypothesis tests [102], set to $K = 4.42$ for an overall significance level of $\alpha = 0.01$ using Z-tests given 924 comparisons.

Considering the inherent randomness in AAFT surrogate generation and to ensure reproducibility, we repeated the entire normalized GSI calculation 100 times for each tissue sample and reported the average normalized GSI value. As demonstrated in Fig 5, the mean measured GSI rapidly stabilizes, converging after approximately 80 iterations. The complete implementation, including scripts for GSI computation and temporal homogenization, is openly available on GitHub: https://github.com/HibaKob/MicroBundleAnalysis. We leverage the results of this analysis in the "Feature correlations reflect both redundancy and novel information" Section.

Average pairwise Dynamic Time Warping (DTW) distance. Originally developed for speech recognition [94,103,104] and later broadly adopted for pattern analysis in diverse time series applications [105–108], Dynamic Time Warping (DTW) distance provides a robust measure of similarity between two temporal sequences that may differ in speed, phase, or timing. Unlike simple distance measures, DTW flexibly aligns sequences by dynamically "warping" the time axis, identifying the optimal path that minimizes the cumulative disparity between corresponding points in the sequences [105]. The resulting DTW distance reflects the total alignment cost, accounting for shifts and stretching along the time dimension.

A key advantage of DTW distance over standard Euclidean distance is its resilience to temporal misalignments. Euclidean-based comparisons are highly sensitive to even minor offsets: for example, if one time series is delayed or shifted relative to another, Euclidean distance will exaggerate their difference despite underlying similarity. In contrast, DTW distance accurately quantifies true similarity by aligning corresponding features, making it especially well-suited for biological time series data where phase variability is common.

In this study, we leverage the DTW distance (Fig 4b-iii) to quantitatively assess waveform heterogeneity within each tissue sample using an average pairwise DTW distance metric. For every tissue, we first normalized each of the three Green-Lagrange strain components (E_{cc}, E_{cr}, and E_{rr}) such that all strain time series amplitudes are scaled between −1 and 1 at each spatial grid location. This normalization ensures meaningful cross-tissue comparisons by removing inter-tissue amplitude differences that could otherwise inflate the DTW metric, while preserving the intrinsic waveform differences among time series within a given tissue. We then computed the DTW distance for every possible pair among the 924 normalized time series per tissue sample, utilizing the Python implementation provided by the DTAIDistance library [109]. The average pairwise DTW distance was defined as follows:

$$\text{average pairwise DTW distance} = \frac{\sum_{i=0}^{N} \sum_{j=0, j \neq i}^{N} \mathrm{DTW}(\mathbf{x}_i, \mathbf{x}_j)}{N(N-1)} \quad (7)$$

where N is the total number of time series per tissue. Interpretively, a lower average pairwise DTW distance indicates that most time series within the tissue are temporally alike, with waveform patterns that align closely even if offset or stretched in time; a higher value signifies greater heterogeneity, capturing pronounced differences in strain dynamics, timing, or shape that persist despite optimal alignment. All code and workflow for calculating the average pairwise DTW distance are openly accessible on GitHub: https://github.com/HibaKob/MicroBundleAnalysis. We present the results of this analysis in the "Feature correlations reflect both redundancy and novel information" Section.

Additional metrics. In addition to the metrics detailed in "Wasserstein distance," "Global synchrony index (GSI)," and "Average pairwise Dynamic Time Warping (DTW) distance" Sections, several informative measures are readily available through the core functionalities of the software tools "MicroBundleCompute" [24] and "MicroBundlePillarTrack" [25]. These common metrics offer complementary insights into fundamental aspects of tissue structure, function, and dynamics and include:

- **Tissue Aspect Ratio** – calculated as the ratio of tissue length to width, with both dimensions extracted from segmented tissue masks. Length is defined as the edge-to-edge distance along the tissue's major axis, while width is measured at the midpoint perpendicular to the major axis.
- **Tissue Curvature** ($1/\mu$m) – quantified as the mean curvature of the two free tissue edges. For each edge, curvature is determined by fitting a circle to the contour points and taking the reciprocal of its radius.
- **Beat Frequency** (Hz) – determined by analyzing the mean absolute displacement time series and calculating the average number of beats per second. Individual beats are identified as intervals between two consecutive valleys (zero-crossings) in the displacement curve.
- **Full Width at Half Maximum (FWHM)** (frames) – measured from the pillar mean absolute displacement time series as the number of frames between the points where displacement amplitude equals half of its peak value (Fig 4b-i).
- **Pillar Mean Peak Force** (μN) – obtained by averaging the absolute peak contraction force measured at each pillar during tissue contraction events.
- **Tissue Mean Peak Absolute Displacement** (pixels) – calculated by taking the mean of the absolute displacement values at maximal contraction across the tissue.
- **Strain Peak Average Asynchrony** (frames) – computed as the mean difference between the frame at which peak mean absolute displacement occurs and the frame of peak Green-Lagrange strain (E_{cc}, E_{cr}, or E_{rr}) at each grid location, providing an aggregate measure of temporal offset across the tissue (Fig 4b-ii).

In this work, displacement-based measurements are reported in pixels rather than physical length units, and temporal measurements are reported in frames rather than physical time units. This choice is justified by the fact that all image sequences in the dataset were acquired under identical imaging settings, at a uniform spatial resolution of 0.908 μm/pixel and an image acquisition rate of 65 Hz. Converting pixel-based displacements to physical units is straightforward: multiplying by the pixel size yields displacements in μm. Similarly, converting frame-based temporal measurements to physical time units requires dividing by the frame rate, which in this case is 65 frames/s, yielding measurements in seconds. Neither conversion alters any comparisons or conclusions within this dataset, as both amount to scaling all values by a constant factor. For cross-platform applicability, however, where imaging settings and pixel sizes may differ across systems, conversion to physical units is recommended to ensure meaningful comparability. The proposed framework readily supports this conversion, provided the pixel size and frame rate of the imaging setup are known.

All code for extracting these direct metrics from our software tools, together with the complete post-processing workflow, is openly available on GitHub: https://github.com/HibaKob/MicroBundleAnalysis. We present the results of these metrics in the "Feature correlations reflect both redundancy and novel information" Section.

Results and discussion

We evaluate the full set of structural, functional, and spatiotemporal metrics defined in the "Materials and methods" Section to determine which features meaningfully characterize cardiac microbundle behavior and which add little additional insight. Rather than assuming all metrics are equally informative, our objective is to assess the choice of metrics

itself and examine how different selections shape the interpretation of the dataset described in the "Dataset" Section, which comprises 20 experimental conditions. Consistent with this objective, we do not pursue mechanistic explanations for condition-dependent differences, but instead focus on an interpretation-agnostic analysis of how the metrics behave across conditions.

We first examine how these metrics vary across the 20 experimental conditions and identify features that remain consistent across fibroTUGs irrespective of condition ("Interpretable features show continuous variation across experimental conditions" Section). We then analyze relationships among metrics to quantify correlations, multicollinearity, and informational overlap, using both statistical measures and machine learning approaches ("Feature correlations reflect both redundancy and novel information" Section). Building on this analysis, we assess how different feature-selection choices influence condition-level comparisons ("Condition-level comparisons depend on the selected feature" Section) and show that multivariate analyses provide important context beyond univariate metrics by clarifying the underlying structure and dispersion of the data across conditions ("Multivariate analysis reveals distinct condition centroids amid broad dispersion" Section).

Interpretable features show continuous variation across experimental conditions

As an initial step, we examined how the 16 extracted interpretable metrics vary across the experimental conditions represented in the dataset. To this end, we applied three complementary dimensionality-reduction techniques: Principal Component Analysis (PCA) [63], Uniform Manifold Approximation and Projection (UMAP) [110], and t-Distributed Stochastic Neighbor Embedding (t-SNE) [111]. While PCA captures dominant linear variance and provides interpretable component loadings, UMAP and t-SNE generate embeddings that emphasize nonlinear and local relationships that may not be resolved by linear projection. Qualitative consistency across these complementary embeddings suggests that the observed patterns are not specific to a single dimensionality-reduction method and thus are more robust.

The resulting embeddings are shown in Fig 6. The condition-labeled projections (Fig 6a) reveal that no method yields perfectly separable groups. PCA shows substantial overlap among conditions, whereas UMAP and t-SNE produce more visually distinct cluster structures. However, these clusters are not exclusive: several conditions appear in multiple clusters, and considerable overlap persists across methods.

Notably, when the embeddings are visualized according to tissue stress at peak contraction (Fig 6b), a broad continuum becomes apparent, with samples graded from low to high stress along the dominant axes of each projection. Rather than forming condition-specific clusters, the data exhibit a smooth transition that organizes fibroTUGs into low-, medium-, and high-stress regimes. This pattern suggests that variation in tissue stress aligns more closely with the underlying structure captured by the metrics than do the discrete experimental labels. More broadly, these observations illustrate the inherent difficulty of analyzing biological systems: measurements are high-dimensional, interdependent, and often reflect continuous biological variation rather than sharply separated groups. As such, interpreting these datasets requires integrative approaches that can account for subtle gradients and shared features across conditions.

Principal Component Analysis uncovers primary isotropic contraction mode in tissue displacement

The PCA detailed in the "Principal component analysis" Section offers novel perspectives on the collective contraction dynamics of the tissues. Examination of vector plots of the first 10 principal components (PCs) (Fig 7) reveals distinct and interpretable spatial deformation patterns. For instance, PC1, which reflects the dominant contraction mode shared across all samples, is indicative of a global isotropic contraction, aligned with the major axis of the tissue. On the other hand, PC2 is principally governed by lateral deformation, while PC3 and PC4 reflect a combination of lateral and anisotropic stretching. Notably, reconstruction using the first 4 PCs accounts for approximately 85% of the observed variance (Fig 8a), underscoring the predominance of linear, non-rotational contractile behavior in governing the motion of these tissues.

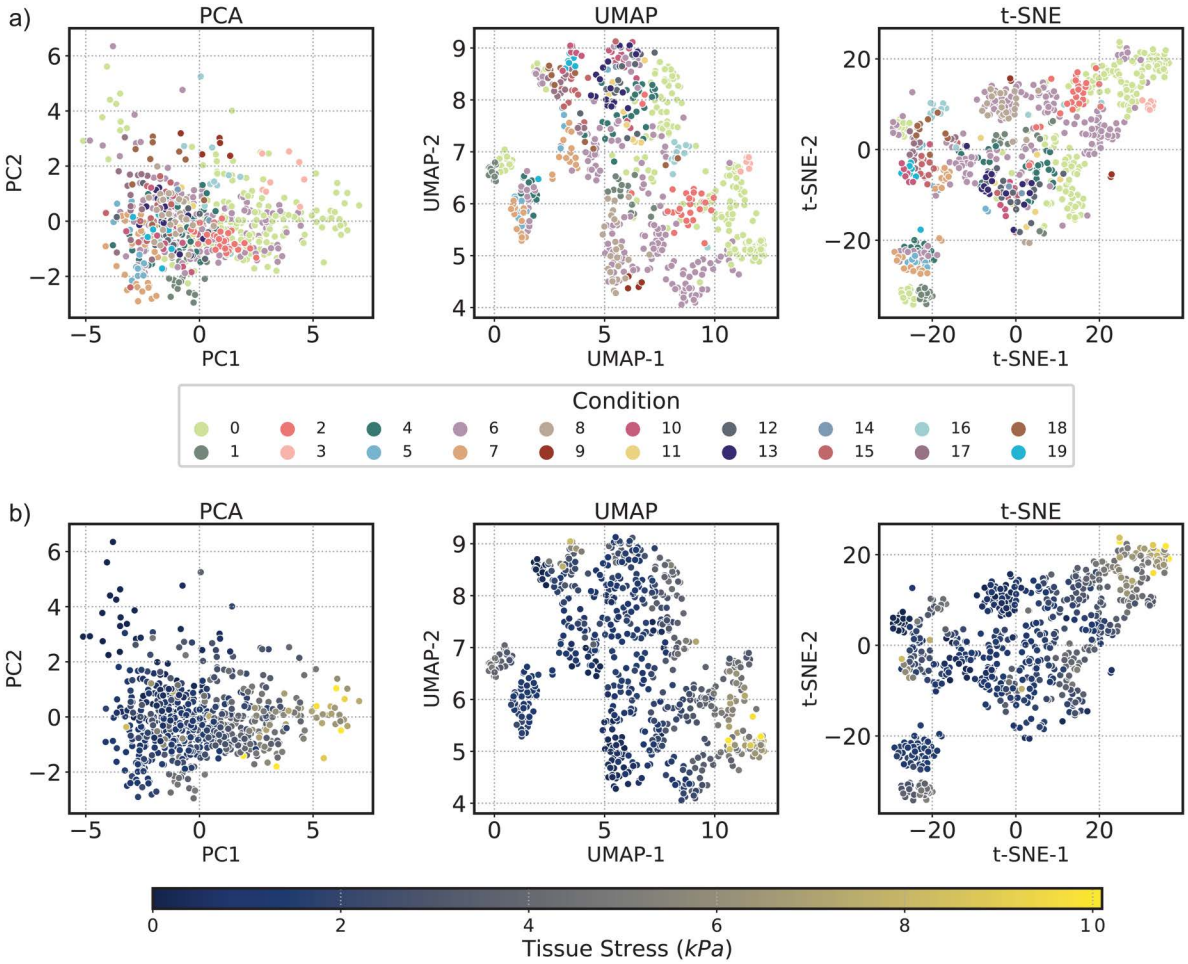


Fig 6. Dimensionality reduction visualizations of the 16 extracted features applied using three methods. PCA (`n_components=2`), UMAP (`n_components=2, n_neighbors=30, min_dist=0.2, spread=1.0, random_state=42`), and t-SNE (`n_components=2, perplexity=30, learning_rate=100, early_exaggeration=12, random_state=42`). Each method is visualized with respect to: (a) the 20 distinct experimental conditions, and (b) peak tissue stress (*kPa*) at maximal contraction, calculated as the ratio of mean peak pillar force to the cross-sectional area at the tissue centroid, approximated as a rectangle. These representations highlight the clustering patterns and dispersion across conditions, as well as the nearly continuous variation of tissue stress across the multidimensional feature space.

https://doi.org/10.1371/journal.pcbi.1014522.g006

Beyond the primary modes, higher order components (PC5 – PC10) capture more intricate and localized displacement patterns, including clear evidence of vortex-like and rotational elements. These PCs introduce spatial heterogeneity, with local undulations, non-linear gradients, and twisting motions that are not embodied in the dominant contraction modes. Such features reflect finer-scale tissue mechanics, encompassing localized contraction and mechanical diversity that contribute incrementally to the overall displacement field. This hierarchical progression, from simpler, coordinated global contraction to increasingly complex and localized dynamics, mirrors the organizational structure of tissue mechanics. Most of the tissue displacement can be explained by a handful of global, coordinated contraction modes; residual variance is distributed among less prominent, spatially complex processes.

Visualizing the dataset in the PC1–PC2 space (Fig 8b, left panel) reveals that dominant contraction patterns identified by PCA transcend experimental conditions, as substantial overlap and a lack of discrete clustering is prevalent. Crucially, projection onto PC1 demonstrates a strong positive linear correlation with measured pillar force (Fig 8b, right panel),

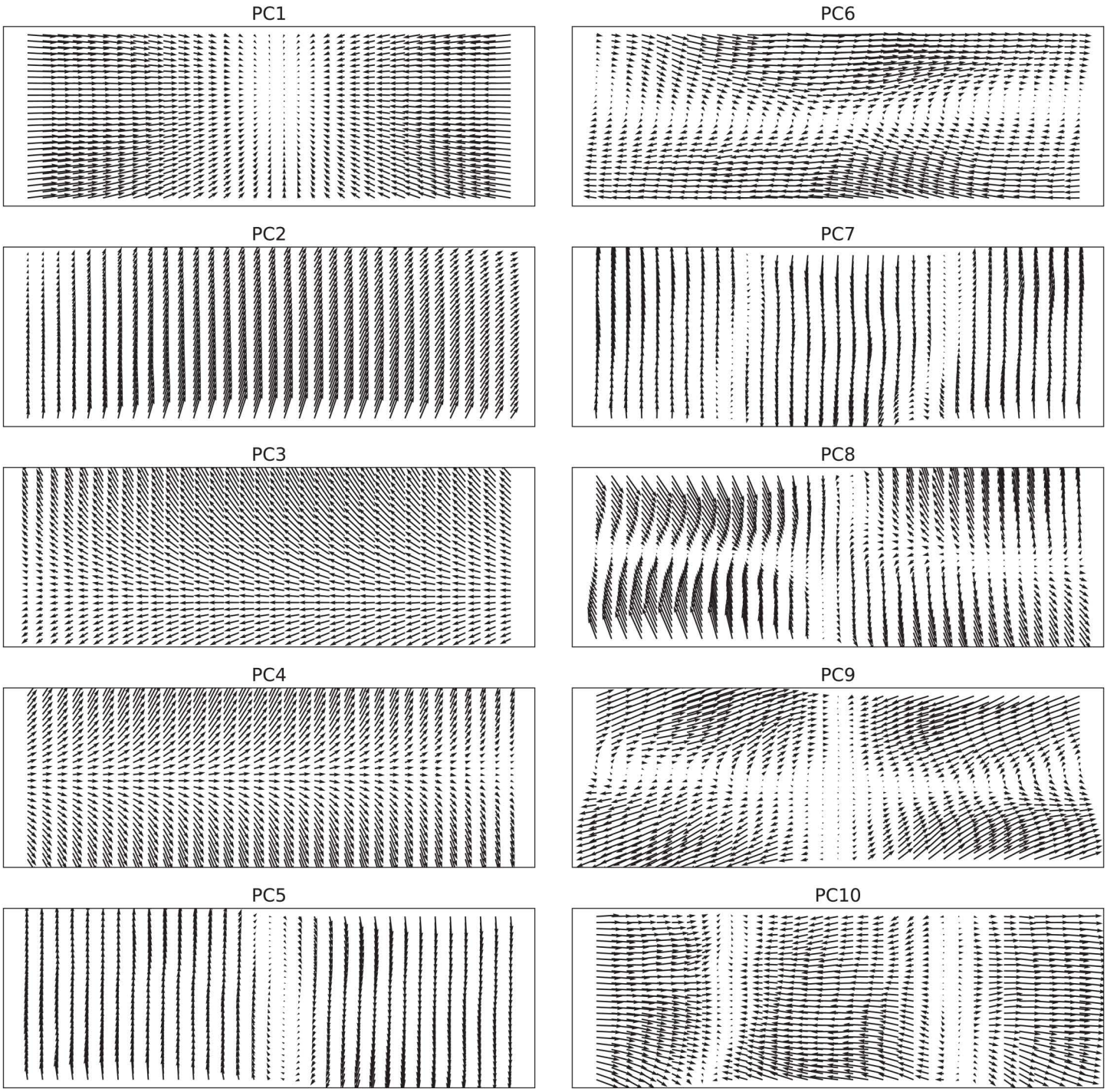


Fig 7. Vector plots illustrating the spatial displacement patterns corresponding to the first 10 principal components derived from PCA performed collectively on the displacement fields of all 670 tissue samples at peak contraction. Each mode captures a dominant pattern of motion present across the dataset, ordered by decreasing explained variance as shown in Fig 8a.

https://doi.org/10.1371/journal.pcbi.1014522.g007

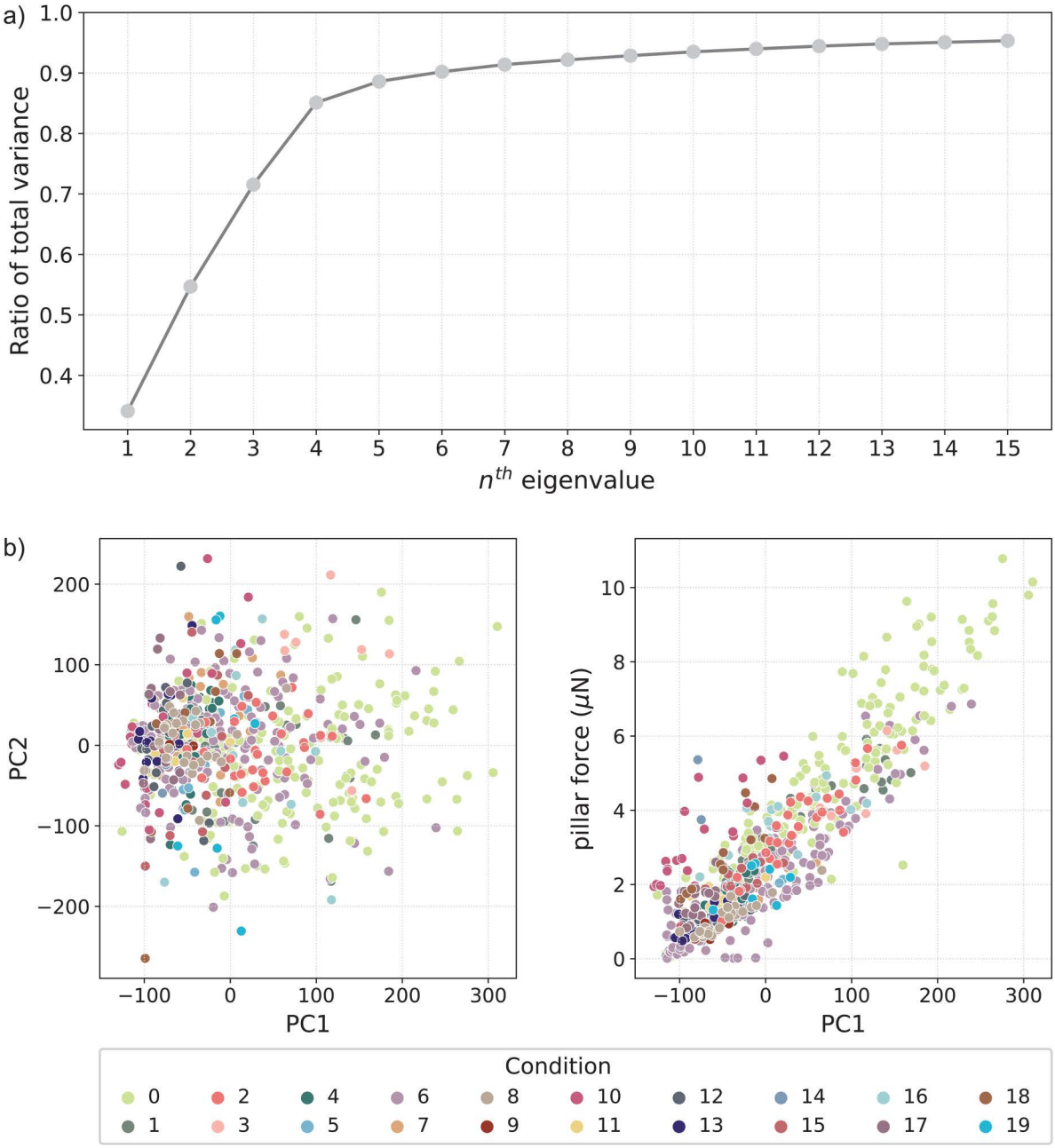


Fig 8. PCA provides additional insight into tissue displacement fields at peak contraction. (a) The cumulative variance plot demonstrates that the first 4 principal components capture approximately 85% of the total variance, indicating that most contraction patterns are efficiently described by a limited number of dominant modes. **(b)** Despite this, visualization in the PC1–PC2 space (left panel) does not reveal clear clustering by experimental condition, highlighting substantial overlap between groups. Notably, the projection onto PC1 exhibits a strong positive linear correlation with measured pillar force (right panel), confirming that the primary mode of displacement, corresponding to isotropic contraction, is highly correlated to increased tissue contraction force across all samples.

https://doi.org/10.1371/journal.pcbi.1014522.g008

confirming that global isotropic contraction along the tissue's major axis acts as a principal driver of elevated contraction force across all samples.

With our analysis, we have only scraped the surface of what an in-depth PCA can reveal. As a starting point, one can apply unsupervised methods, such as clustering on PC scores, to identify new patterns across samples. Another immediate exploration is to extend PCA to dynamic analyses and apply temporal or spatiotemporal PCA to sequences of displacement fields over time, revealing how tissue contraction dynamics evolve. In future studies, which would require the generation of new experimental data, it would also be possible to specifically investigate the biological and experimental determinants of each PC. For instance, one can combine PCA insights with additional data modalities, such as gene expression, protein levels, or tissue composition to test if specific PCs are predictive of key outcomes of, for example, tissue viability, maturation, or pathological states.

Furthermore, the principal directions identified through PCA could serve as valuable benchmarks for both validating and informing computational models of fibroTUG tissues [112,113]. Rather than relying solely on one-to-one comparisons of displacement field magnitudes, the dominant deformation vector patterns extracted via PCA offer a robust framework for assessing whether computational models accurately reproduce the essential modes of tissue behavior. Importantly, these principal patterns can reveal critical aspects such as global fiber orientations and the spatial distribution of contraction sites, allowing for targeted refinement of model parameters. By integrating PCA-derived insights, computational models can be iteratively calibrated to better capture the complex structural and functional characteristics observed in experimental data.

Critical point analysis provides complementary insights to PCA

As detailed in the "Critical point analysis" Section, we performed a critical point analysis on the reconstructed displacement fields of all 670 tissue samples, using the first 10 principal components. The results, summarized in Fig 9 and Table 1, show that saddle point patterns are frequently observed but not ubiquitous. Of note, this dataset is evenly divided between examples exhibiting saddle points and those with no critical points at all. Representative vector field patterns illustrating both scenarios are shown in Fig 9a and 9b.

A closer examination also reveals substantial variation in the prevalence of saddle points across experimental conditions. As visualized in Fig 9c, certain conditions, such as 1, 5, and 6, demonstrate a relatively high incidence of saddle point patterns, while others, notably 14 and 18, display none. This heterogeneity suggests that the occurrence of saddle points is, to a limited extent, condition-dependent and may be modulated by other underlying experimental variables or intrinsic tissue properties. Further investigations, which may require integrating additional experimental variables, are needed to clarify the drivers of this heterogeneity and its biological implications.

While PCA highlights dominant modes of contraction, the critical point analysis uncovers local spatial heterogeneities and complex deformation patterns that are not captured by variance-based dimensionality reduction alone. This underscores the potential value of integrating topological analysis with PCA to better characterize spatiotemporal contraction dynamics. A promising direction for future critical point analysis involves tracking the temporal dynamics of these features, enabling us to observe how critical points arise, migrate, or vanish throughout the tissue contraction cycles. Such an approach could shed light on the mechanical evolution and stability of tissue regions during active deformation. Additionally, a thorough investigation of the spatial organization of critical points would be valuable, for instance, assessing whether their distribution is random or exhibits clustering within specific tissue domains. This could reveal underlying mechanical microenvironments and potential hotspots of activity. Here, mechanical microenvironments refer to spatially distinct regions experiencing different local mechanical conditions, arising from variations in matrix stiffness, fiber alignment, cell density, or sarcomere organization, while hotspots of activity refer to regions where significant mechanical events are concentrated, such as areas of locally elevated deformation or strain. Most intriguingly, integrating critical point information with high-resolution immunostained imaging would enable the investigation of potential co-localization

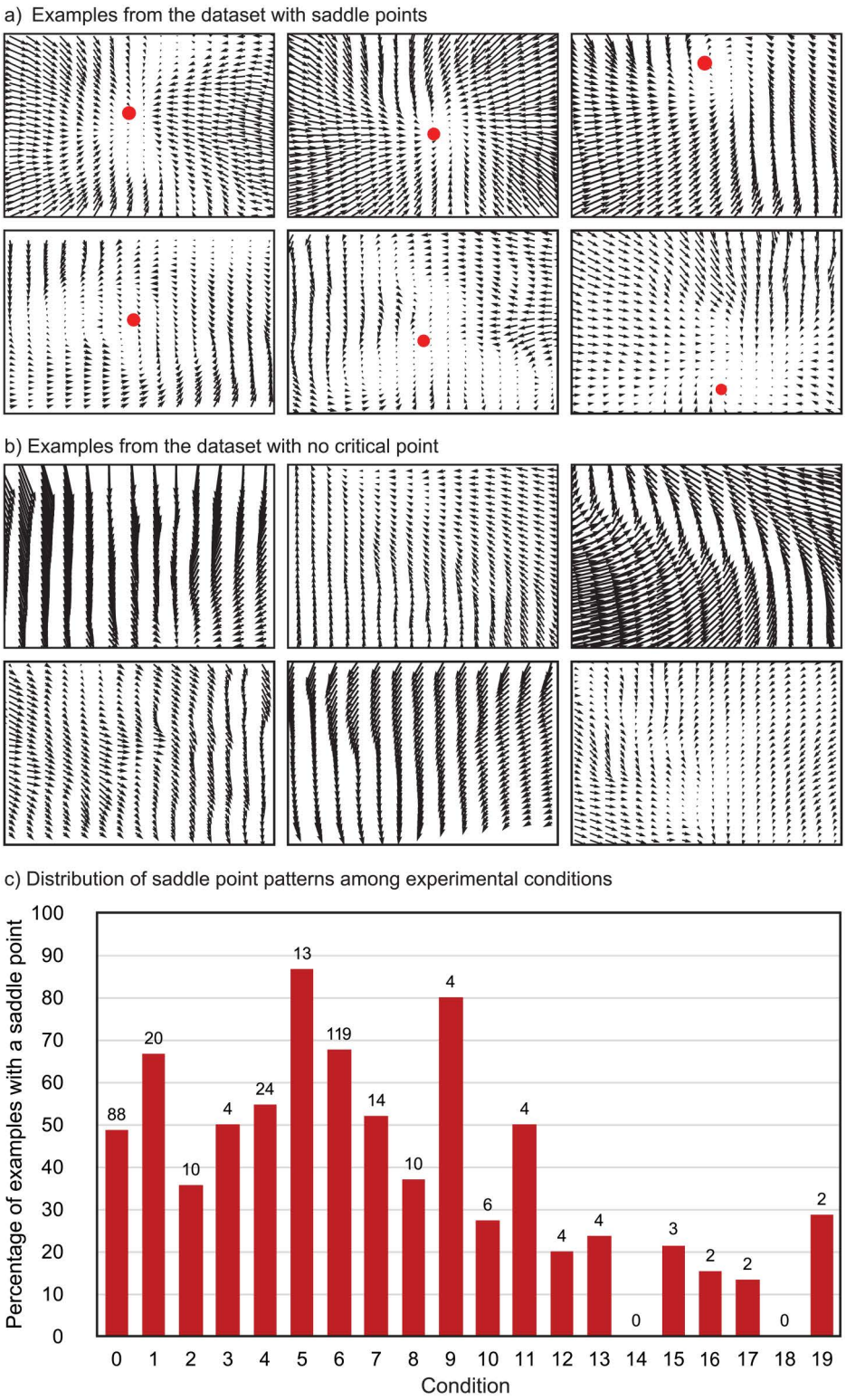


Fig 9. Schematic overview of the critical point analysis results. (a) Representative examples from the dataset exhibiting saddle points in the displacement field, with saddle locations indicated by red dots. **(b)** Examples from the dataset that lack any identified critical points, illustrating alternative

contraction or deformation patterns. **(c)** The occurrence of saddle point patterns varies across experimental conditions, and no experimental conditions exclusively yield saddle points. Numbers above each bar indicate the absolute count of examples featuring a saddle point within each condition. For completeness, we note that condition 14 contains only 2 examples whereas condition 18 contains 11 examples.

https://doi.org/10.1371/journal.pcbi.1014522.g009

Table 1. Summary of critical point analysis results for all 670 tissue samples, detailing the type and frequency of observed critical points. The analysis reveals an equal division between examples exhibiting saddle point patterns (333) and those with no detected critical points (333).

type	saddle point	stable node	unstable node	stable focus	unstable focus	center point	absence of critical point
frequency	333	3	0	1	0	0	333

https://doi.org/10.1371/journal.pcbi.1014522.t001

between critical points and the underlying cellular architecture and tissue composition. This multimodal analysis could uncover important mechanistic links between topological features in displacement fields and the biological makeup of the tissue, paving the way for new insights into tissue structure-function relationships. Furthermore, drug perturbation studies represent a promising avenue for directly probing the biological mechanisms underlying critical point behavior, as pharmacological interventions could reveal how changes in cellular contractility and organization influence the emergence and spatial distribution of these topological features.

Feature correlations reflect both redundancy and novel information

Interrelationships and redundancy among extracted metrics. We next investigated the relationships among the extracted metrics in order to assess their informational value and identify potential redundancy. Our goal was to determine whether all metrics are essential, or if some exhibit sufficiently high inter-correlation to warrant exclusion. To this end, we evaluated multicollinearity among the metrics using two complementary measures: the condition number, which provides an overall assessment of collinearity, and the variance inflation factor (VIF), which pinpoints the specific sources. [114].

The condition number is derived as the maximum of the condition indices, which themselves are computed from the eigenvalues (λ) of the scaled correlation (or covariance) matrix of the remaining metrics in a regression model as $\text{condition index}_i = \sqrt{(\lambda_{\max}/\lambda_i)}$ where λ_i are the eigenvalues of the correlation matrix of the predictors, and $\lambda_{\max}$ is the largest eigenvalue. Then for each metric, VIF is calculated as $\text{VIF}_i = 1/(1 - R_i^2)$, where R_i^2 is the coefficient of multiple determination from regressing metric *i* against the remaining metrics.

Commonly accepted thresholds for weak collinearity are a condition number less than 10 and VIF values below 5 [114]. Table 2 summarizes the multicollinearity analysis. The results demonstrate that, while the complete set of 16 metrics displays weak global collinearity (condition number below 10), certain strain-derived metrics exhibit elevated VIF values. When metrics related to E_{cr} and E_{rr} are excluded, both the condition number and variance inflation factors for the remaining metrics drop well below critical thresholds–except for “Tissue Mean Peak Absolute Displacement” and “Pillar Mean Peak Force”–suggesting minimal collinearity. Based on this assessment, we restrict our downstream analyses to the 10 key metrics identified in Table 2.

As a next step, we investigated pairwise relationships among all metrics. We first calculated the Spearman’s rank correlation coefficient (ρ) [115], which captures monotonic relationships regardless of linearity, for every metric pair. Recognizing, as Anscombe’s quartet [116] exemplifies, that summary statistics alone can mask nuanced patterns in the data, we complemented the correlation analysis with pairplots for each metric combination to visually examine their associations. In addition, we included Kernel Density Estimate (KDE) plots to assess the distribution and variability of each metric. The width of the KDE curve reflects the degree of variability: wider curves indicate greater variance, while narrow curves suggest more closely grouped observations. Moreover, skewness in the KDE curves may indicate data asymmetry or the presence of outliers.

Table 2. Multicollinearity was assessed using condition number and variance inflation factor. Collinearity is generally low, with condition numbers for both the full set of 16 metrics (8.04) and the 10 selected metrics (5.67) well below the threshold of 10. The 10 selected metrics are highlighted in bold font. Notable multicollinearity is confined to strain-derived metrics; excluding those linked to E_{cr} and E_{rr} yields consistently low VIF values for the remaining metrics, except for "Tissue Mean Peak Absolute Displacement" and "Pillar Mean Peak Force," which are highly inter-correlated.

Metric	Variance Inflation Factor	
Tissue Aspect Ratio	1.40	1.32
Tissue Curvature	1.11	1.10
Beat Frequency	3.63	2.91
Tissue Mean Peak Absolute Displacement	5.11	4.91
Pillar Mean Peak Force	7.28	5.00
Full Width at Half Maximum	2.38	2.16
Wasserstein Distance PC10	3.02	2.70
Ecc Strain Peak Average Asynchrony	19.05	1.11
Ecr Strain Peak Average Asynchrony	22.93	–
Err Strain Peak Average Asynchrony	15.04	–
Ecc Average Pairwise DTW Distance	3.07	2.01
Ecr Average Pairwise DTW Distance	3.90	–
Err Average Pairwise DTW Distance	2.84	–
Ecc GSI	7.54	3.12
Ecr GSI	3.87	–
Err GSI	2.80	–
Condition number	**8.04**	**5.67**

https://doi.org/10.1371/journal.pcbi.1014522.t002

To streamline interpretation and avoid redundancy inherent in symmetric correlation matrices, we condensed the results in Fig 10, focusing on the 10 representative metrics with minimal collinearity identified in Table 2. The figure is organized as a 10×10 matrix: the diagonal elements feature KDE plots illustrating each metric's distribution, the upper triangle displays Spearman's correlation coefficients, and the lower triangle contains pairplots visualizing the relationships. Comprehensive results for all 16 metrics are similarly presented in S3 Fig.

Surveying the matrix, the upper triangle reveals that most metric pairs show negligible ($|\rho| < 0.3$) or weak ($0.3 \leq |\rho| < 0.5$) monotonic associations [117,118], suggesting that the metrics largely capture distinct aspects of tissue behavior. Moderate ($0.5 \leq |\rho| < 0.7$) and strong ($0.7 \leq |\rho| < 0.9$) correlations are relatively rare and limited to several metric clusters. Noteworthy examples of strong positive correlations include "Tissue Mean Peak Absolute Displacement," "Pillar Mean Peak Force," "Wasserstein Distance PC10," and "E_{cc} GSI." In contrast, "Beat Frequency," "Full Width at Half Maximum," and "E_{cc} Average Pairwise DTW Distance" form a cluster of negative correlations. Nevertheless, perfect correlations are absent; the strongest observed Spearman coefficient is between "Tissue Mean Peak Absolute Displacement" and "Pillar Mean Peak Force" ($\rho = 0.826$), underscoring that each metric retains unique informational value.

The KDE plots along the diagonal confirm that metrics such as "Tissue Curvature" and "E_{cc} Strain Peak Average Asynchrony" are relatively consistent across conditions, while others like "Pillar Mean Peak Force" and "Full Width at Half Maximum" display greater variability and occasional outliers. The pairplots in the lower triangle further validate the absence of pronounced non-monotonic or anomalous relationships, providing visual confirmation that the data structure is well-represented by the computed Spearman correlations.

Prediction-based assessment of metric redundancy. To provide an alternative perspective on metric redundancy, we designed an exhaustive prediction-based strategy using machine learning methods. From the set of 10 metrics, we selected one as a held-out target and used the remaining 9 metrics as input features for prediction. For these 9

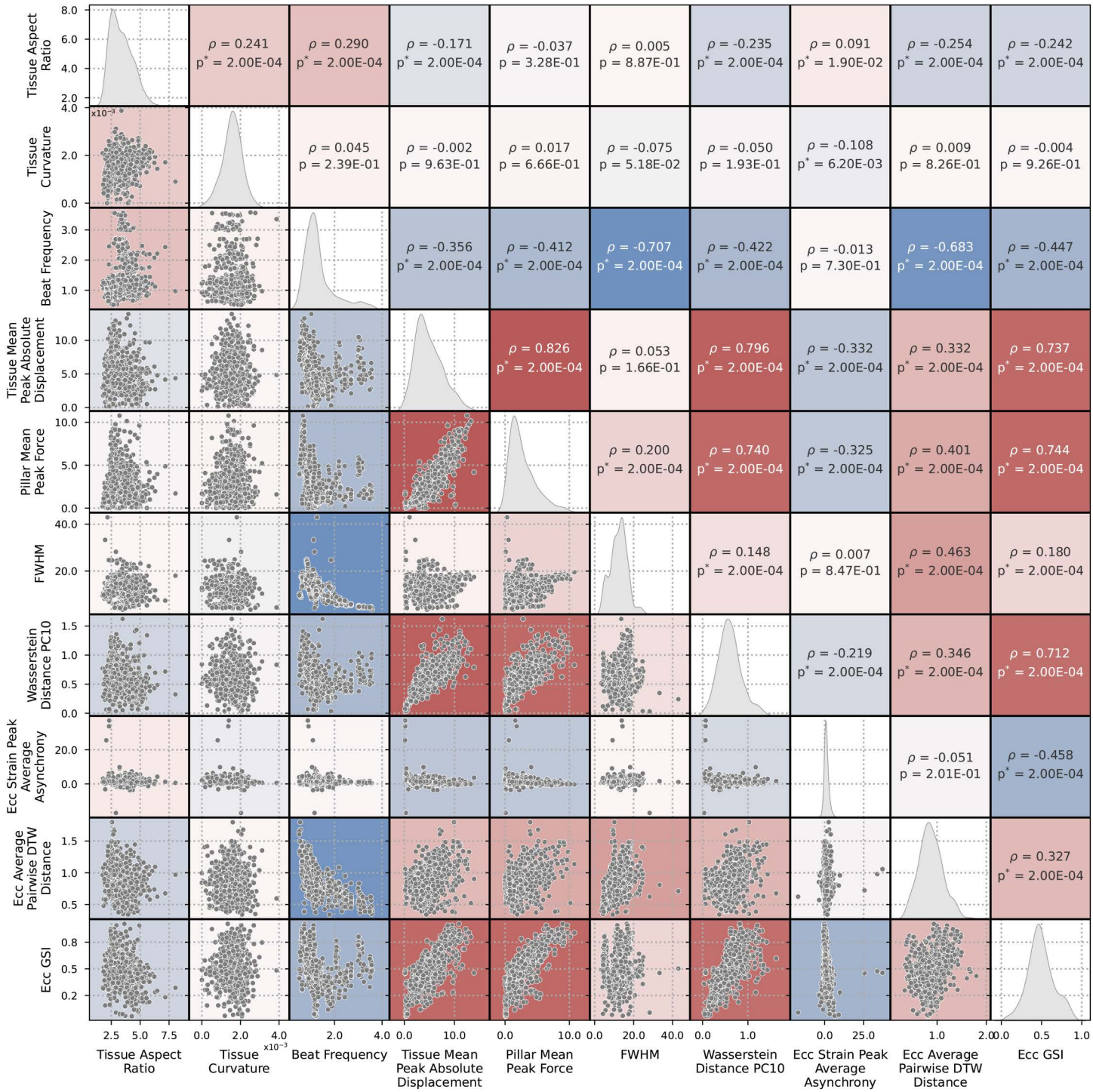


Fig 10. Comprehensive visualization of pairwise relationships among metrics. The upper triangle displays Spearman's correlation coefficients (ρ) along with the corresponding p-values, providing both the strength and statistical significance of monotonic associations between metrics. The lower triangle features pairplots that visualize the joint distribution of each metric pair. Kernel Density Estimate (KDE) plots along the diagonal illustrate the distribution of individual metrics, highlighting variation in data spread.

https://doi.org/10.1371/journal.pcbi.1014522.g010

metrics, we considered all possible feature combinations of size k ($k \in [1, 9]$), resulting in a total of 511 unique subsets ($\sum_{k=1}^{9} {}_9C_k$). For each subset, we trained a multilayer perceptron (MLP) using the scikit-learn Python library (v1.7.1) [71], employing a parameter grid search to optimize model depth (up to three layers) and the hyperparameters `alpha` and `learning_rate_init`, selecting the configuration with the lowest validation loss. Fixed common hyperparameters include `activation='relu'`, `solver='adam'`, `num_epochs=1000`, `patience=15`, `lr_patience=8`, `decay_factor=0.5`, and `random_state=42`. The dataset was split into 60%, 20%, and 20% for training, validation, and test, respectively. This analysis was performed for two representative metrics with notably high inter-correlation and elevated VIF values: "Pillar Mean Peak Force" and "E_{cc} GSI."

The outcomes of this predictive analysis are summarized in Fig 11, where we evaluated the reconstruction accuracy using the R^2 score on the test dataset. Each outcome is color-coded based on the highest Spearman's correlation coefficient identified among the input features. In general, we observed that the predictive performance improves as the number of input features increases, particularly when those features include variables with strong Spearman correlation to the held-out metric. This trend demonstrates that access to more relevant features enhances the model's ability to capture the underlying structure of the data. However, after a certain point, the addition of more features yields only marginal gains, and the R^2 curve plateaus. This plateauing effect indicates that once the most influential variables have been incorporated into the model, further expansion of the input set provides diminishing returns, highlighting redundancy among certain features. For example, a model trained with 2 metrics, with one being "Tissue Mean Peak Absolute Displacement," can predict "Pillar Mean Peak Force" with a similar accuracy to one trained on all 9 features.

This analysis reveals intricate, non-linear relationships between metrics that transcend the scope of standard correlation measures. Importantly, subsets of features with moderate maximum Spearman correlation ($0.5 < |\rho_{max}| < 0.7$) can still achieve substantial predictive accuracy. Future studies employing larger datasets, rigorously defined metrics, and advanced machine learning techniques will be pivotal in disentangling the connections among diverse tissue

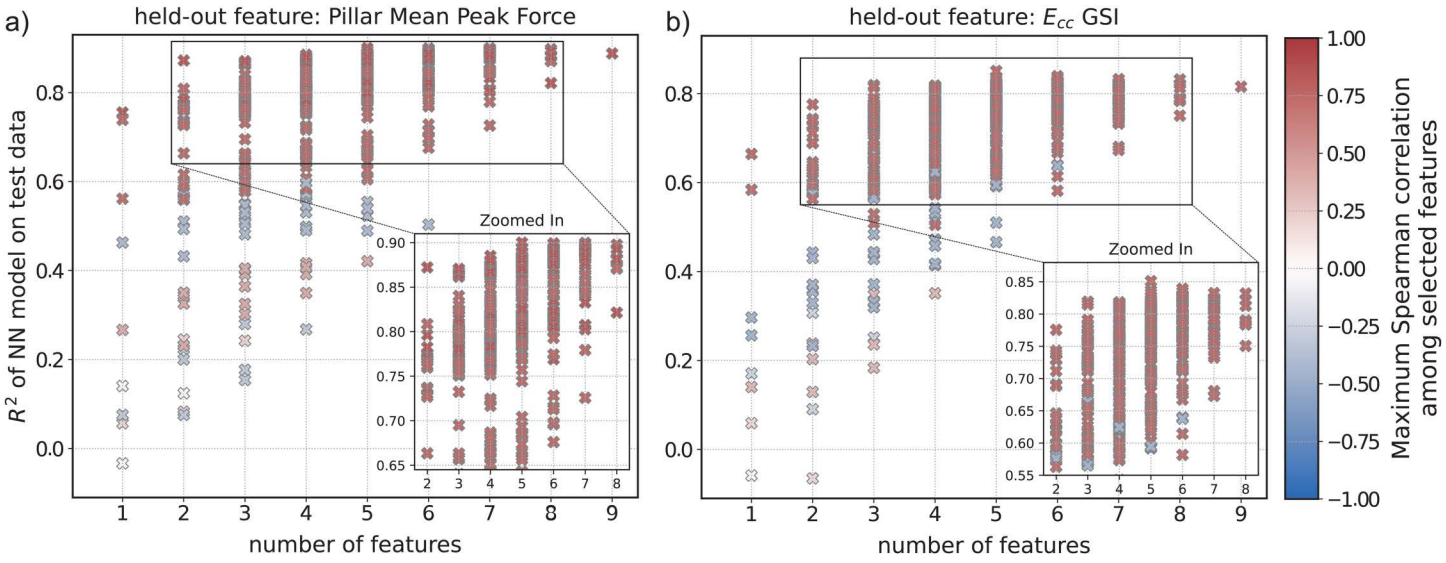


Fig 11. Summary of prediction performance for all multilayer perceptron (MLP) models. These models were trained using different numbers and combinations of input features, with **(a)** "Pillar Mean Peak Force" and **(b)** "E_{cc} GSI" held out as target variables. For each case, the R^2 value of the neural network on test data is shown as a function of the number of input features. Results are color-coded according to the maximum Spearman's correlation coefficient observed among the selected input features, highlighting the impact of feature inter-correlation on model performance. Insets provide a closer view of regions with higher R^2.

https://doi.org/10.1371/journal.pcbi.1014522.g011

characteristics, such as the links between structural properties and heterogeneous contractile function. Such approaches can also help determine the minimum set of metrics required for comprehensive characterization of tissue dynamics. Ultimately, these strategies will provide critical insights for experimental design and support more informed and targeted investigations.

Condition-level comparisons depend on the selected feature

In this section, we investigate whether the choice of metric influences the analysis outcome. Our approach builds on the correlation and redundancy analyses presented in the "Feature correlations reflect both redundancy and novel information" Section, which motivated the use of the reduced set of 10 metrics. From the 20 experimental conditions, we retained only 7 with more than 25 samples to ensure adequate statistical power and meaningful comparisons for this component of our analysis.

To select a suitable statistical framework, we considered several key properties of our data: metric distributions are generally non-normal, group variances are unequal, and sample sizes vary across conditions. Additionally, our analyses require comparison across multiple groups for each metric. Given these characteristics, the Kruskal–Wallis H test [119] is well-suited for our needs. As a nonparametric, rank-based method, it serves as an alternative to one-way ANOVA for comparing 3 or more independent samples. The interpretation of the Kruskal–Wallis test [119] depends heavily on the underlying distributions of the observations [120]: when group distributions differ markedly, the test assesses stochastic dominance; if distributions are identical, it tests for differences in medians; and with symmetric distributions, it tests for mean differences. In our context, the metric distributions across the 7 conditions (Figs 12c and S4 Figb) are neither identical nor symmetric; hence, we interpret the Kruskal–Wallis test results as reflecting differences in stochastic dominance among conditions.

To complement the assessment of statistical significance ($p < 0.05$), we also report an effect size ϵ^2 [121], defined as $\epsilon^2 = (H - k + 1)/(N - 1)$, where H is the Kruskal–Wallis statistic, k is the number of conditions ($k = 7$), and N is the total number of tissue samples ($N = 513$). Following the guidelines in [122], values of $0.01 \leq \epsilon^2 < 0.06$ indicate a small effect, $0.06 \leq \epsilon^2 < 0.14$ a medium effect, and $\epsilon^2 > 0.14$ a large effect.

Because a significant Kruskal–Wallis result does not identify which specific groups differ, we follow up with Dunn's test which compares mean ranks for stochastic dominance [123] among multiple pairwise post-hoc comparisons. To control for type I errors arising from multiple testing, we apply the Holm–Bonferroni correction [124].

We present the results of this analysis in Fig 12. Fig 12a summarizes the condition Kruskal–Wallis mean rankings for each metric, where favorable ranks are positioned at the top. For clarity of interpretation, the metrics are ordered such that higher-ranked values correspond to more desirable outcomes. For instance, distance-based metrics are arranged in ascending order, where smaller distances are favored, reflecting an assumed preference for homogeneous tissue, whereas force-related metrics are ordered in descending fashion, reflecting the desirability of higher force generation.

At the top of the chart, Kruskal–Wallis effect sizes (ϵ^2) are displayed for each metric, with statistically significant results marked by an asterisk. Most metrics exhibit large effect sizes, with the exception of "E_{cc} Strain Peak Average Asynchrony," which shows a medium effect, and "Tissue Curvature," which shows a small effect. Each circular marker (Fig 12a) denotes the median metric value for that condition. Generally, rankings by median and Kruskal–Wallis mean rank are in agreement; however, any discrepancies highlight underlying non-standard distributions–such as multimodality, skewness, or outliers–where the mean rank offers a more accurate comparative ordering. For example, although condition 0 has a higher median "E_{cc} GSI" than condition 2, its rank is lower, which aligns with the relatively bimodal and skewed distribution seen in "E_{cc} GSI" for condition 0 (see S4 Figb).

When comparing how conditions rank across individual metrics (Fig 12a), we observe notable consistency among the first 3, "Tissue Mean Peak Absolute Displacement," "Pillar Mean Peak Force," and "E_{cc} GSI," for which the relative ordering of conditions remains largely stable. This alignment suggests that conditions producing greater tissue displacement or

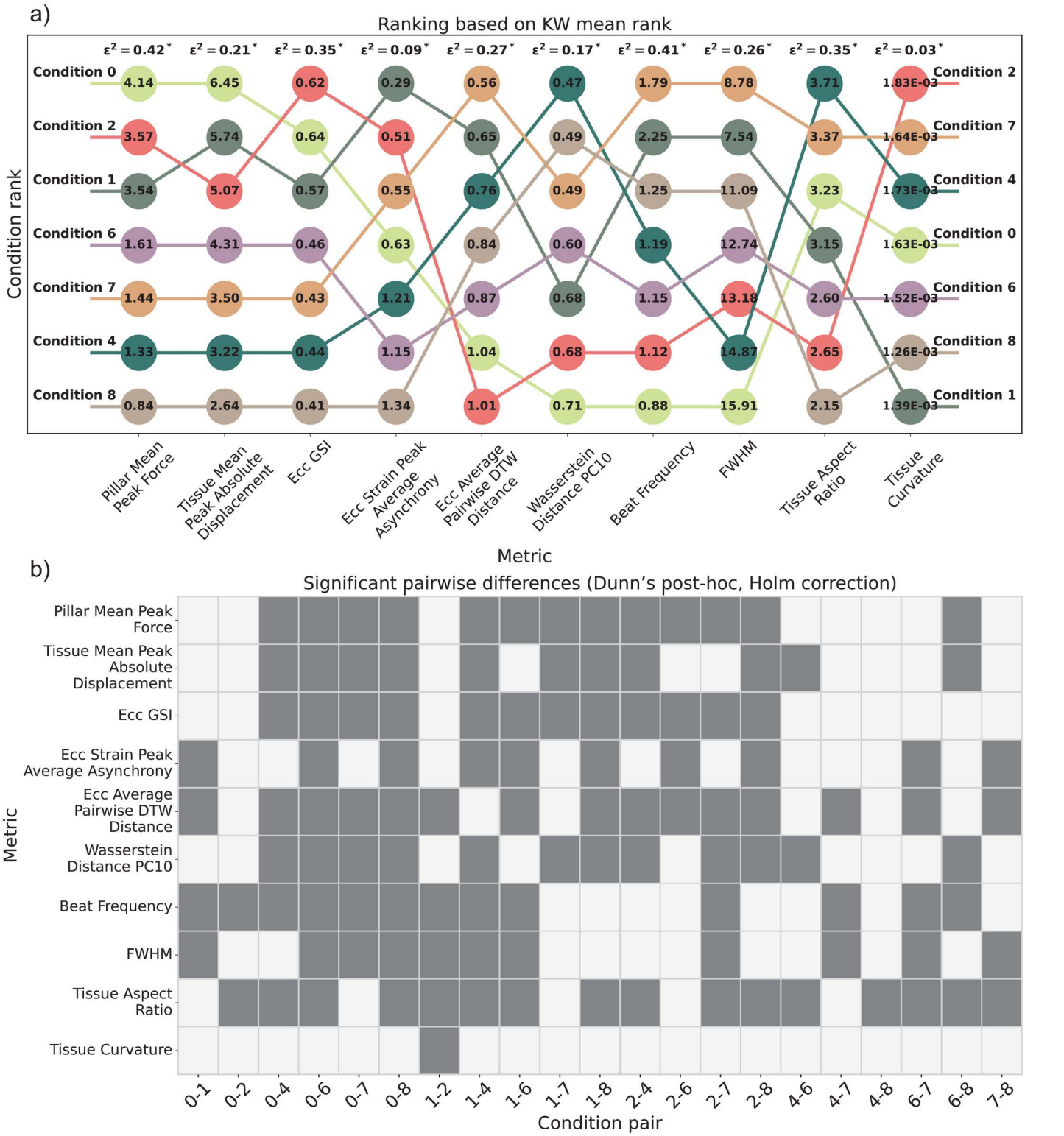


Fig 12. Statistical comparison of selected features across experimental conditions. (a) bump chart showing condition rankings based on Kruskal–Wallis mean rank with feature median values displayed within the circle markers. Kruskal–Wallis effect sizes (ϵ^2) are summarized above each feature,

with asterisks indicating statistical significance. Ranking order (ascending or descending) is based on each metric's favorable direction; (b) binary matrix of significant pairwise differences between condition pairs identified by Dunn's post-hoc test with Holm–Bonferroni correction, where dark grey cells indicate comparisons with $p < 0.05$.

https://doi.org/10.1371/journal.pcbi.1014522.g012

contraction also tend to generate higher forces and exhibit more globally synchronized beating. In contrast, the rankings diverge considerably for the remaining metrics. For instance, conditions 0 and 2, which appear highly favorable according to the first 3 metrics, move to the bottom of the ranking when evaluated using "E_{cc} Average Pairwise DTW Distance," "Wasserstein Distance PC10," "Beat Frequency," and "Full Width at Half Maximum." This shift indicates that, despite exhibiting strong temporal synchrony, tissues under these conditions display more heterogeneous strain time series profiles across spatial regions, produce displacement vector fields that deviate more from the low-dimensional reconstruction based on the first 10 principal components, beat at higher frequencies, and exhibit broader beat profiles. Thus, the choice of metric can substantially alter the outcome of the comparison, at times leading to contrasting interpretations of condition favorability.

These observations must be interpreted in conjunction with the statistical significance of pairwise comparisons obtained from the Holm-corrected Dunn's test [123,124] (Fig 12b). The results reveal that certain condition pairs exhibit virtually no significant differences across any metric, for example, pairs $0-2$, $4-8$, whereas others, such as $0-6$ and $0-8$, differ significantly on nearly all metrics. In this context, the apparent ranking of conditions 0, 1, and 2 for "Tissue Mean Peak Absolute Displacement," "Pillar Mean Peak Force," and "E_{cc} GSI" does not hold statistical support: the pairwise differences among these conditions are not significant.

Note on the dangers of analytical flexibility. A critical implication of our statistical analysis is the risk of inadvertently engaging in data dredging, or p-hacking [125]. This occurs when researchers explore a wide array of analytical choices such as varying the selection of variables, data subsets, or preprocessing decisions, and selectively report only those results that achieve statistical significance. In our dataset, this risk may take the form of highlighting only significant findings, repeatedly modifying data-cleaning criteria (for example, removing or retaining outliers), or performing multiple subgroup analyses but disclosing only those yielding p-values below 0.05. Notably, these behaviors may arise inadvertently rather than from intentional misconduct. Nevertheless, they undermine statistical validity and inflate the likelihood of false positives, presenting spurious outcomes as genuine discoveries.

In the present work, our aim is not to advance specific biological conclusions but to illustrate, in a conclusion-agnostic manner, the potential range of analytical comparisons that can be performed with these types of data, and highlight the methodological considerations that accompany them. As larger and more complex datasets become increasingly common, we encourage researchers to carefully document and justify key analytical decisions, consider pre-specifying their primary analysis strategy (for example, through preregistration), and transparently report relevant analytical alternatives where practical. Such practices need not require exhaustive reporting of every possible analysis, but fostering transparency in the analytical workflow can help minimize false discoveries and strengthen the reproducibility and robustness of scientific findings [126–128].

Multivariate analysis reveals distinct condition centroids amid broad dispersion

As a final example of what is possible with these additional metrics, we examined how the combined features differ across experimental conditions using Permutational Multivariate Analysis of Variance (PERMANOVA) [129]. PERMANOVA is a nonparametric test that evaluates whether multivariate observations differ between groups based on a chosen distance matrix. Unlike MANOVA [130], it does not require multivariate normality and is widely used with skewed, sparse, or zero-inflated data. The method partitions the total sum of squares in the distance matrix and assesses group differences by permuting group labels to construct a null distribution for the pseudo-F statistic.

However, PERMANOVA is sensitive to differences in both group centroids and group dispersions. To evaluate whether groups differ in their multivariate dispersion, defined as the average distance of observations to their group centroid, we

also applied PERMDISP (Permutational Analysis of Multivariate Dispersions) [129]. Interpreting PERMANOVA together with PERMDISP provides a more nuanced understanding of the multivariate structure: significant PERMANOVA results in the absence of dispersion differences suggest genuine centroid shifts, whereas significant dispersion differences indicate that variation in group spread may contribute to or even drive the observed group separation.

For this analysis, we focused on the reduced set of 10 metrics across the 7 selected experimental conditions defined in the "Condition-level comparisons depend on the selected feature" Section. PERMANOVA was implemented in Python using the `scikit-bio` library [131], with Euclidean distances computed after standardizing the data. To ensure robust statistical inference, we used 59,999 permutations with a fixed random seed of 123. Pairwise PERMANOVA tests were conducted for all condition combinations, and the Holm–Bonferroni method [124] was applied to correct for multiple comparisons. The results are summarized in Figs 13 and S4 Fig.

Fig 13a displays the PERMANOVA outputs, including the pseudo-F statistic (the ratio of between-group to within-group mean squares obtained by partitioning sums of squares derived from the distance matrix), the explained variation R^2 (the proportion of distance-based variation explained by group membership), and the associated p-values. All condition pairs exhibit statistically significant differences in their multivariate distance structures, with pairs $2-8$, $0-6$, $0-7$, and $2-4$ exhibiting the highest pseudo-F values. As for R^2 values, they ranged from 0.023 to 0.494, indicating that condition explained approximately 2.3% to 49.4% of the pairwise multivariate variation. The highest R^2 values were observed for the pairs $2-8$, $2-7$, $1-8$, and $2-4$. These findings indicate that although group differences are statistically significant, the effect sizes vary substantially across condition pairs, with condition explaining only a small fraction of the total multivariate structure in some comparisons and nearly half in others.

To further interpret the PERMANOVA findings, we supplemented our analysis with PERMDISP (Permutational Analysis of Multivariate Dispersions), also implemented using `scikit-bio` [131] (S4 Figa). PERMDISP tests whether groups differ in their multivariate dispersion, defined as the average distance of observations to their respective group centroids. Combining the results of PERMANOVA and PERMDISP leads to four primary scenarios. For descriptive clarity, R^2=0.15 was used to separate lower-magnitude comparisons from the larger observed pairwise differences in this dataset:

1. **Significant PERMANOVA, lower R^2, and non-significant PERMDISP** (pairs: $0-1$, $0-6$, $1-6$, $4-7$, $6-7$):

In these cases, dispersions do not differ significantly across groups, and the significant PERMANOVA result is therefore most consistent with a detectable but relatively small shift in group centroids rather than dispersion-driven effects.

2. **Significant PERMANOVA, higher R^2, and non-significant PERMDISP** (pairs: $0-7$, $1-4$, $1-7$, $2-8$):

In these cases, dispersions do not differ significantly across groups, and the significant PERMANOVA result is therefore most consistent with differences in multivariate location. These pairs show more pronounced condition-associated differences, with the largest value observed for pair 2–8, where condition explained approximately 49.4% of the pairwise multivariate variation.

3. **Significant PERMANOVA, lower R^2, and significant PERMDISP** (pairs: $0-2$, $0-4$, $0-8$, $2-6$, $4-6$, $4-8$, $6-8$):

In these pairs, groups differ in dispersion, and condition explains a relatively small fraction of the pairwise multivariate variation. Consequently, the significant PERMANOVA result may be partly or entirely driven by heterogeneous spread rather than differences in centroid location alone. Interpretations of group separation should therefore be made with caution, because dispersion differences can inflate or mimic significance in PERMANOVA.

4. **Significant PERMANOVA, higher R^2, and significant PERMDISP** (pairs: $1-2$, $1-8$, $2-4$, $2-7$, $7-8$):

In these pairs, condition explains a larger fraction of the pairwise multivariate variation, but groups also differ in dispersion. These comparisons therefore indicate pronounced differences in multivariate mechanical distributions, but the

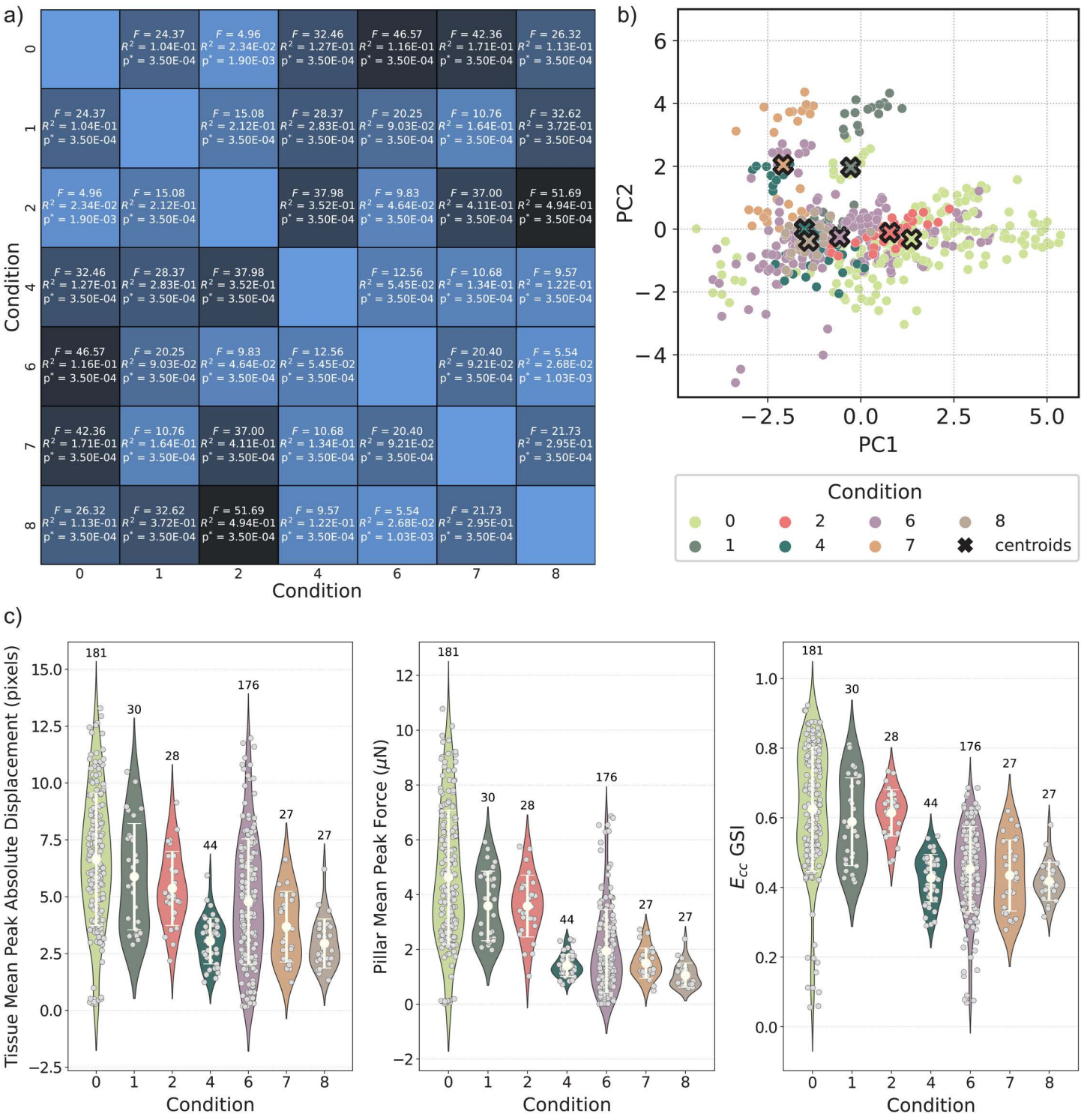


Fig 13. Multivariate statistical analysis across experimental conditions. (a) Annotated heatmap of PERMANOVA results, with darker blue shades indicating higher pseudo-*F* statistics; R^2 and p-values are also displayed for each condition pair with an asterisk denoting statistical significance. **(b)** Principal component projection (PC1 vs. PC2) of the dataset comprising the 10 metrics and 7 conditions, with data points color-coded by condition and

centroids marked for each group. **(c)** Violin plots of 3 representative metrics, "Tissue Mean Peak Absolute Displacement," "Pillar Mean Peak Force," and "E_{cc} GSI," showing mean ± standard deviation for each condition.

https://doi.org/10.1371/journal.pcbi.1014522.g013

differences cannot be attributed solely to centroid shifts because heterogeneous spread may also contribute to the PERMANOVA significance.

To visually explore these patterns, we performed a principal component analysis (PCA) on the tissue examples using the 10 metrics. Fig 13b shows the data projected onto the first two principal components, color-coded by condition. This visualization shows separated condition centroids (with the exceptions of pairs 0 – 2 and 4 – 8, which are closer in space), but extensive overlap and large dispersion within each condition exists, underscoring the effects observed in the PERMANOVA and PERMDISP results.

Additionally, Fig 13c displays violin plots for three representative metrics: "Tissue Mean Peak Absolute Displacement," "Pillar Mean Peak Force," and "E_{cc} GSI." These visualizations, together with the complementary violin plots for the remaining seven metrics in S4 Figb, help contextualize the multivariate statistical findings. For example, the condition pair 0 – 2 ($F = 4.96$, $R^2 = 0.023$, PERMANOVA; $F = 43.82$, PERMDISP, both statistically significant) exhibits a large difference in within-group dispersion and only modest condition-associated variation in multivariate space. In contrast, the pair 2 – 8 ($F = 51.69$, $R^2 = 0.494$, PERMANOVA, statistically significant; $F = 0.17$, PERMDISP, not significant) shows clear separation between group centroids with relatively similar within-group dispersions, with condition explaining nearly half of the pairwise multivariate variation.

Conclusion

In this work, we present a computational pipeline for quantifying dynamic behavior in brightfield videos of beating cardiac microbundles, leveraging and expanding our open-source tools "MicroBundleCompute" [24] and "MicroBundlePillarTrack" [25]. We introduce 16 metrics that capture heterogeneous spatiotemporal contractility by integrating structural and functional features with hybrid spatial and temporal descriptors, and we apply them to a dataset of 670 cardiac tissues spanning 20 experimental conditions on the fibroTUG platform [20,39]. Through statistical and machine learning analyses, we assess the relevance, redundancy, and necessity of each metric and identify a core subset required to effectively characterize tissue behavior. Dimensionality reduction methods (PCA, UMAP, t-SNE) show that no combination of metrics perfectly separates experimental conditions, underscoring the inherent biological complexity of this system. Analysis of denoised displacement fields further reveals that tissue contraction is primarily linear and isotropic along the major axis, with saddle points present in approximately 50% of samples, an observation that warrants deeper investigation into the relationship between contractile patterns and microstructure.

Investigation of metric interrelationships showed that multicollinearity and redundancy are limited. After reducing the strain-derived metrics by retaining only the E_{cc} component, a refined set of 10 metrics captured the majority of the informational value. Correlations among metrics were mostly weak to moderate, with the strongest Spearman coefficient ($\rho = 0.826$) observed between "Tissue Mean Peak Absolute Displacement" and "Pillar Mean Peak Force" and the weakest between "Tissue Curvature" and "E_{cc} GSI" ($\rho = -0.004$). Machine learning models further supported this conclusion by demonstrating that predictive accuracy improves when correlated features are included, but only up to a point, indicating that redundancy among metrics is modest. These results also highlight that quantitative interpretations can vary depending on the specific metrics used, particularly when comparing across experimental conditions. Multivariate analyses revealed that within-condition dispersion often exceeds between-condition separation, underscoring the need for cautious interpretation when drawing biological conclusions. Collectively, our analytical framework provides a robust and reproducible approach for the comprehensive study of cardiac microtissue contractility across diverse experimental scenarios, and

the full Python implementation is openly available on GitHub (https://github.com/HibaKob/MicroBundleAnalysis) to support broad adoption and continued development.

While our framework was applied to a single cardiac tissue platform, the methodology is readily extensible to time-lapse imaging of cardiac tissues across a variety of experimental setups and modalities where approximating full-field deformation is feasible [31,48–51]. These approaches can be adapted to other engineered tissue types, such as the actuated two-dimensional muscle sheets described in [132]. The meaningfulness of such analyses, however, will depend critically on the quality of the underlying imaging data and tracking algorithm performance. It is therefore recommended to verify that foundational imaging and tracking requirements are met prior to applying this framework to new experimental platforms or imaging conditions, where factors such as potential refractive index variations during tissue contraction may warrant additional consideration.

Moving forward, analyses leveraging this comprehensive suite of metrics can guide the design of more rigorous and comparable experiments, enabling the identification of optimal culture conditions and configurations that enhance hiPSC-CM tissue maturation. Specifically, a well-powered longitudinal study with balanced sample numbers across multiple culture ages would further validate the utility of these metrics as maturity indicators by capturing the progression of contractile behavior toward a stable and mature phenotype. Collectively, these efforts will facilitate reproducible extraction of mechanical phenotypes across diverse testbeds and directly inform the development of improved computational models of engineered tissues.

A promising direction for future work is to integrate these dynamic metrics with detailed structural descriptors obtained from fluorescent staining and complementary imaging modalities, such as calcium imaging. This integrated approach could address important questions, such as how much predictive power can be gained from easily obtained structural metrics derived from still images, or how structural organization, ranging from sarcomere geometry and alignment to the broader architecture of the extracellular matrix and cell arrangement, influences contractile function. Ultimately, these investigations may help determine whether brightfield imaging alone captures sufficient information to characterize tissue behavior, or whether complementary modalities are necessary. In particular, it will be valuable to evaluate if synchrony metrics like the GSI can provide robust functional insights using only brightfield data. While this remains a challenging question, it presents a compelling avenue for advancing tissue engineering research.

A limitation of the present study is that it analyzes 2D time-lapse image sequences and therefore quantifies projected in-plane tissue motion rather than full 3D deformation. Although the tissue platforms considered here and in prior validation studies include quasi-3D and 3D engineered cardiac tissues, the current implementation does not reconstruct volumetric displacement or strain fields. Several components of the framework, including spatial registration, dimensionality reduction, and synchrony analysis, could be extended to 3D volumetric time-lapse data, while others, such as strain reconstruction and critical point analysis, would require methodological adaptation. Given that high-resolution volumetric imaging with sufficient temporal resolution for beating engineered tissues remains technically challenging, the present work focuses on scalable analysis of 2D time-lapse imaging data, with future extensions to fully 3D spatiotemporal datasets as imaging technologies mature.

In summary, the pipeline and metrics developed in this work contribute a versatile and extensible toolkit for the quantitative analysis of engineered tissue dynamics. By making these methods openly available, we hope to accelerate discovery, facilitate cross-platform comparisons, and inspire innovative experiments in the field of cardiac tissue engineering and beyond.

Supporting information

S1 Fig. Details of computing a Green-Lagrange strain field from tracked displacement data. The left panel shows the absolute displacement field at peak contraction, obtained at the tracked fiducial marker points and interpolated onto a 28×33 regular grid; the zoomed-in inset highlights the spatial distribution of fiducial marker points within the tissue

domain. Directional displacement fields in the column (horizontal) and row (vertical) directions are obtained analogously. The locations of the tracked fiducial marker points in both the reference (undeformed) and current (deformed) configurations serve as the input to the strain computation illustrated in the middle panel. There, a *k*-nearest neighbor approach is used to estimate the local deformation gradient at each fiducial marker point. For a given marker point α (here shown with $k = 8$ neighbors), the vectors $\mathbf{X}^{\alpha\beta}$ and $\mathbf{x}^{\alpha\beta}$ connect point α to each neighbor β in the reference and current configurations, respectively. The deformation gradient tensor $\mathbf{F}^{\alpha}$ is estimated from these neighbor vectors via a least-squares fitting procedure, and the Green-Lagrange strain tensor $\mathbf{E}^{\alpha}$ is subsequently computed as shown. Repeating this procedure at every fiducial marker point yields the full-field strain estimate shown in the right panel, where the Green-Lagrange strain in the column-column direction E_{cc} is displayed at all fiducial marker points and interpolated onto the 28×33 regular grid. Positive and negative values indicate local extension and compression, respectively, as indicated by the color scale.
(PDF)

S2 Fig. Grid sensitivity analysis for all grid-dependent metrics. (a) Example of a tissue-specific 13×22 interpolation grid used for displacement and strain calculations, with a zoomed-in view. For our main analysis, a finer 28×33 grid is applied. Subplots (b–f) compare metric values computed on both grid resolutions, demonstrating convergence with increasing grid size. While most metrics show strong agreement (high r^2 values) between grids, "E_{cc} Average Pairwise DTW Distance" exhibits greater sensitivity to grid resolution. Based on these results, the 28×33 grid provides sufficient resolution for robust metric calculations.
(PDF)

S3 Fig. Expanded version of Fig 10 displaying all 16 extracted metrics. The upper triangle presents the Spearman's correlation coefficients (ρ) for each metric pair, accompanied by their respective p-values. The lower triangle contains pairplots depicting the joint distributions for each pair of metrics, providing further support for the monotonicity assumption underlying the Spearman correlation analysis. Along the diagonal, Kernel Density Estimate (KDE) plots illustrate the individual distribution of each metric, highlighting differences in data spread and underlying variability across metrics.
(PDF)

S4 Fig. Multivariate statistical analysis across experimental conditions. (a) Annotated heatmap of PERMDISP results, where deeper blue tones represent higher pseudo-*F* statistics. P-values are shown for each condition pair, with an asterisk indicating statistical significance. (b) Violin plots for the remaining 7 metrics from Fig 12, depicting the distribution, mean, and standard deviation for each condition.
(PDF)

Acknowledgments

We thank Boston University Research Computing Services for providing the computational infrastructure and tools that enabled the analyses reported here. We are also grateful to Professor Paul Barbone for his insightful feedback and guidance on principal component analysis.

Author contributions

Conceptualization: Hiba Kobeissi, Emma Lejeune.

Data curation: Hiba Kobeissi, Emma Lejeune.

Formal analysis: Hiba Kobeissi, Emma Lejeune.

Funding acquisition: David Nordsletten, Brendon M. Baker, Emma Lejeune.

Investigation: Hiba Kobeissi, Samuel J. DePalma, Emma Lejeune.

Methodology: Hiba Kobeissi, Emma Lejeune.

Project administration: Hiba Kobeissi, Emma Lejeune.

Resources: David Nordsletten, Brendon M. Baker, Emma Lejeune.

Software: Hiba Kobeissi, Emma Lejeune.

Supervision: David Nordsletten, Brendon M. Baker, Emma Lejeune.

Validation: Hiba Kobeissi, Javiera Jilberto, Emma Lejeune.

Visualization: Hiba Kobeissi, Emma Lejeune.

Writing – original draft: Hiba Kobeissi, Emma Lejeune.

Writing – review & editing: Hiba Kobeissi, Samuel J. DePalma, Javiera Jilberto, David Nordsletten, Brendon M. Baker, Emma Lejeune.

References

1. De Chiara F, Ferret-Miñana A, Fernández-Costa JM, Ramón-Azcón J. The Tissue Engineering Revolution: From Bench Research to Clinical Reality. Biomedicines. 2024;12(2):453. https://doi.org/10.3390/biomedicines12020453 PMID: 38398055
2. Hoang VT, Nguyen QT, Phan TTK, Pham TH, Dinh NTH, Anh LPH. Tissue Engineering and Regenerative Medicine: Perspectives and Challenges. MedComm. 2025;6(5):e70192. https://doi.org/10.1002/mco2.70192
3. Lian X, Hsiao C, Wilson G, Zhu K, Hazeltine LB, Azarin SM, et al. Robust cardiomyocyte differentiation from human pluripotent stem cells via temporal modulation of canonical Wnt signaling. Proc Natl Acad Sci U S A. 2012;109(27):E1848-57. https://doi.org/10.1073/pnas.1200250109 PMID: 22645348
4. Burridge PW, Matsa E, Shukla P, Lin ZC, Churko JM, Ebert AD, et al. Chemically defined generation of human cardiomyocytes. Nat Methods. 2014;11(8):855–60. https://doi.org/10.1038/nmeth.2999 PMID: 24930130
5. Eldeeb AE, Salah S, Elkasabgy NA. Biomaterials for Tissue Engineering Applications and Current Updates in the Field: A Comprehensive Review. AAPS PharmSciTech. 2022;23(7):267. https://doi.org/10.1208/s12249-022-02419-1 PMID: 36163568
6. Ketabat F, Alcorn J, Kelly ME, Badea I, Chen X. Cardiac Tissue Engineering: A Journey from Scaffold Fabrication to In Vitro Characterization. Small Sci. 2024;4(9):2400079. https://doi.org/10.1002/smsc.202400079 PMID: 40212070
7. De Pieri A, Rochev Y, Zeugolis DI. Scaffold-free cell-based tissue engineering therapies: advances, shortfalls and forecast. NPJ Regen Med. 2021;6(1):18. https://doi.org/10.1038/s41536-021-00133-3 PMID: 33782415
8. Cho S, Discher DE, Leong KW, Vunjak-Novakovic G, Wu JC. Challenges and opportunities for the next generation of cardiovascular tissue engineering. Nat Methods. 2022;19(9):1064–71. https://doi.org/10.1038/s41592-022-01591-3 PMID: 36064773
9. Dou W, Malhi M, Zhao Q, Wang L, Huang Z, Law J, et al. Microengineered platforms for characterizing the contractile function of in vitro cardiac models. Microsyst Nanoeng. 2022;8:26. https://doi.org/10.1038/s41378-021-00344-0 PMID: 35299653
10. Ouyang W, Zimmer C. The imaging tsunami: Computational opportunities and challenges. Curr Opin Syst Biol. 2017;4:105–13. https://doi.org/10.1016/j.coisb.2017.07.011
11. Ashammakhi N, GhavamiNejad A, Tutar R, Fricker A, Roy I, Chatzistavrou X, et al. Highlights on Advancing Frontiers in Tissue Engineering. Tissue Eng Part B Rev. 2022;28(3):633–64. https://doi.org/10.1089/ten.TEB.2021.0012 PMID: 34210148
12. Kalkunte N, Cisneros J, Castillo E, Zoldan J. A review on machine learning approaches in cardiac tissue engineering. Front Biomater Sci. 2024;3. https://doi.org/10.3389/fbiom.2024.1358508
13. Zhuang RZ, Lock R, Liu B, Vunjak-Novakovic G. Opportunities and challenges in cardiac tissue engineering from an analysis of two decades of advances. Nat Biomed Eng. 2022;6(4):327–38. https://doi.org/10.1038/s41551-022-00885-3 PMID: 35478227
14. Ewoldt JK, DePalma SJ, Jewett ME, Karakan MÇ, Lin Y-M, Mir Hashemian P, et al. Induced pluripotent stem cell-derived cardiomyocyte in vitro models: benchmarking progress and ongoing challenges. Nat Methods. 2025;22(1):24–40. https://doi.org/10.1038/s41592-024-02480-7 PMID: 39516564
15. Luo L, Okur KE, Bagnaninchi PO, El Haj AJ. Current challenges in imaging the mechanical properties of tissue engineered grafts. Front Biomater Sci. 2024;3:1323763. https://doi.org/10.3389/fbiom.2024.1323763
16. Du J, Yang Y-C, An Z-J, Zhang M-H, Fu X-H, Huang Z-F, et al. Advances in spatial transcriptomics and related data analysis strategies. J Transl Med. 2023;21(1):330. https://doi.org/10.1186/s12967-023-04150-2 PMID: 37202762
17. Grases D, Porta-Pardo E. A practical guide to spatial transcriptomics: lessons from over 1000 samples. Trends Biotechnol. 2025. https://doi.org/10.1016/j.tibtech.2025.08.020

18. Hirt MN, Hansen A, Eschenhagen T. Cardiac tissue engineering: state of the art. Circ Res. 2014;114(2):354–67. https://doi.org/10.1161/CIRCRESAHA.114.300522 PMID: 24436431
19. Sarkans U, Chiu W, Collinson L, Darrow MC, Ellenberg J, Grunwald D, et al. REMBI: Recommended Metadata for Biological Images-enabling reuse of microscopy data in biology. Nat Methods. 2021;18(12):1418–22. https://doi.org/10.1038/s41592-021-01166-8 PMID: 34021280
20. Kobeissi H, Gao X, DePalma SJ, Ewoldt JK, Wang MC, Das SL, et al. FibroTUG platforms: Time-lapse microscopy dataset of engineered cardiac microbundles. 2024. Available from: https://doi.org/10.5061/dryad.3r2280gqd
21. Kobeissi H, Gao X, DePalma SJ, Ewoldt JK, Wang MC, Das SL, et al. Strain gauge platforms: Time-lapse microscopy dataset of engineered cardiac microbundles. 2024. Available from: https://doi.org/10.5061/dryad.sqv9s4nbg
22. Iudin A, Korir PK, Somasundharam S, Weyand S, Cattavitello C, Fonseca N, et al. EMPIAR: the Electron Microscopy Public Image Archive. Nucleic Acids Res. 2023;51(D1):D1503–11. https://doi.org/10.1093/nar/gkac1062 PMID: 36440762
23. Mohammadzadeh S, Tsan Y-C, Kobeissi H, Lejeune E, Helms A. SarcGraph - 2D Cardiac Muscle Bundle. Harvard Dataverse. 2025. https://doi.org/10.7910/DVN/GHMKWJ
24. Kobeissi H, Jilberto J, Karakan MÇ, Gao X, DePalma SJ, Das SL, et al. MicroBundleCompute: Automated segmentation, tracking, and analysis of subdomain deformation in cardiac microbundles. PLoS One. 2024;19(3):e0298863. https://doi.org/10.1371/journal.pone.0298863 PMID: 38530829
25. Kobeissi H, Gao X, DePalma SJ, Ewoldt JK, Wang MC, Das SL, et al. MicroBundlePillarTrack: A Python package for automated segmentation, tracking, and analysis of pillar deflection in cardiac microbundles. MicroPubl Biol. 2024;2024. https://doi.org/10.17912/micropub.biology.001231 PMID: 39114859
26. Huebsch N, Loskill P, Mandegar MA, Marks NC, Sheehan AS, Ma Z, et al. Automated Video-Based Analysis of Contractility and Calcium Flux in Human-Induced Pluripotent Stem Cell-Derived Cardiomyocytes Cultured over Different Spatial Scales. Tissue Eng Part C Methods. 2015;21(5):467–79. https://doi.org/10.1089/ten.TEC.2014.0283 PMID: 25333967
27. Sala L, van Meer BJ, Tertoolen LGJ, Bakkers J, Bellin M, Davis RP, et al. MUSCLEMOTION: A Versatile Open Software Tool to Quantify Cardiomyocyte and Cardiac Muscle Contraction In Vitro and In Vivo. Circ Res. 2018;122(3):e5–16. https://doi.org/10.1161/CIRCRESAHA.117.312067 PMID: 29282212
28. Ronaldson-Bouchard K, Yeager K, Teles D, Chen T, Ma S, Song L, et al. Engineering of human cardiac muscle electromechanically matured to an adult-like phenotype. Nat Protoc. 2019;14(10):2781–817. https://doi.org/10.1038/s41596-019-0189-8 PMID: 31492957
29. Toepfer CN, Sharma A, Cicconet M, Garfinkel AC, Mücke M, Neyazi M, et al. SarcTrack: an adaptable software tool for efficient large-scale analysis of sarcomere function in hiPSC-cardiomyocytes. Circ Res. 2019;124(8):1172–83. https://doi.org/10.1161/CIRCRESAHA.118.314505
30. Psaras Y, Margara F, Cicconet M, Sparrow AJ, Repetti GG, Schmid M, et al. CalTrack: High-Throughput Automated Calcium Transient Analysis in Cardiomyocytes. Circ Res. 2021;129(2):326–41. https://doi.org/10.1161/CIRCRESAHA.121.318868 PMID: 34018815
31. Tsan Y-C, DePalma SJ, Zhao Y-T, Capilnasiu A, Wu Y-W, Elder B, et al. Physiologic biomechanics enhance reproducible contractile development in a stem cell derived cardiac muscle platform. Nat Commun. 2021;12(1):6167. https://doi.org/10.1038/s41467-021-26496-1 PMID: 34697315
32. Tamargo MA, Nash TR, Fleischer S, Kim Y, Vila OF, Yeager K, et al. milliPillar: A Platform for the Generation and Real-Time Assessment of Human Engineered Cardiac Tissues. ACS Biomater Sci Eng. 2021;7(11):5215–29. https://doi.org/10.1021/acsbiomaterials.1c01006 PMID: 34668692
33. Rivera-Arbeláez JM, Keekstra D, Cofiño-Fabres C, Boonen T, Dostanić M, Ten Den SA, et al. Automated assessment of human engineered heart tissues using deep learning and template matching for segmentation and tracking. Bioeng Transl Med. 2023;8(3):e10513. https://doi.org/10.1002/btm2.10513 PMID: 37206226
34. Rivera-Arbeláez JM, Dostanić M, Windt LM, Stein JM, Cofiño-Fabres C, Boonen T, et al. FORCETRACKER: A versatile tool for standardized assessment of tissue contractile properties in 3D Heart-on-Chip platforms. PLoS One. 2025;20(2):e0314985. https://doi.org/10.1371/journal.pone.0314985 PMID: 39946364
35. Mohammadzadeh S, Lejeune E. Quantifying HiPSC-CM structural organization at scale with deep learning-enhanced SarcGraph. PLoS Comput Biol. 2025;21(10):e1013436. https://doi.org/10.1371/journal.pcbi.1013436 PMID: 41042829
36. Mohammadzadeh S, Tsan Y-C, Renberg A, Kobeissi H, Helms A, Lejeune E. SarcGraph for High-Throughput Regional Analysis of Sarcomere Organization and Contractile Function in 2D Cardiac Muscle Bundles. MicroPubl Biol. 2025;2025:10.17912/micropub.biology.001937. https://doi.org/10.17912/micropub.biology.001937 PMID: 41523749
37. Woodhams LG, Guo J, Schuftan D, Boyle JJ, Pryse KM, Elson EL, et al. Virtual blebbistatin: A robust and rapid software approach to motion artifact removal in optical mapping of cardiomyocytes. Proc Natl Acad Sci U S A. 2023;120(38):e2212949120. https://doi.org/10.1073/pnas.2212949120 PMID: 37695908
38. Lebert J, Ravi N, Kensah G, Christoph J. Real-Time Optical Mapping of Contracting Cardiac Tissues With GPU-Accelerated Numerical Motion Tracking. Front Cardiovasc Med. 2022;9:787627. https://doi.org/10.3389/fcvm.2022.787627 PMID: 35686036
39. DePalma SJ, Jilberto J, Stis AE, Huang DD, Lo J, Davidson CD, et al. Matrix Architecture and Mechanics Regulate Myofibril Organization, Costamere Assembly, and Contractility in Engineered Myocardial Microtissues. Adv Sci (Weinh). 2024;11(47):e2309740. https://doi.org/10.1002/advs.202309740 PMID: 39558513
40. Wilkinson MD, Dumontier M, Aalbersberg IJJ, Appleton G, Axton M, Baak A, et al. The FAIR Guiding Principles for scientific data management and stewardship. Sci Data. 2016;3:160018. https://doi.org/10.1038/sdata.2016.18 PMID: 26978244

41. Bertram MG, Sundin J, Roche DG, Sánchez-Tójar A, Thoré ES, Brodin T. Open science. Curr Biol. 2023;33(15):R792-7. https://doi.org/10.1016/j.cub.2023.05.036
42. National Academies of Sciences, Engineering, and Medicine. Open science by design: Realizing a vision for 21st century research. The National Academies Press; 2018. https://doi.org/10.17226/25116
43. Kemmer I, Keppler A, Serrano-Solano B, Rybina A, Özdemir B, Bischof J, et al. Building a FAIR image data ecosystem for microscopy communities. Histochem Cell Biol. 2023;160(3):199–209. https://doi.org/10.1007/s00418-023-02203-7 PMID: 37341795
44. Schapiro D, Yapp C, Sokolov A, Reynolds SM, Chen Y-A, Sudar D, et al. MITI minimum information guidelines for highly multiplexed tissue images. Nat Methods. 2022;19(3):262–7. https://doi.org/10.1038/s41592-022-01415-4 PMID: 35277708
45. Hosseini R, Vlasveld M, Willemse J, van de Water B, Le Dévédec SE, Wolstencroft KJ. FAIR High Content Screening in Bioimaging. Sci Data. 2023;10(1):462. https://doi.org/10.1038/s41597-023-02367-w PMID: 37460560
46. Davidson CD, Jayco DKP, Matera DL, DePalma SJ, Hiraki HL, Wang WY, et al. Myofibroblast activation in synthetic fibrous matrices composed of dextran vinyl sulfone. Acta Biomater. 2020;105:78–86. https://doi.org/10.1016/j.actbio.2020.01.009 PMID: 31945504
47. DePalma SJ, Davidson CD, Stis AE, Helms AS, Baker BM. Microenvironmental determinants of organized iPSC-cardiomyocyte tissues on synthetic fibrous matrices. Biomater Sci. 2021;9(1):93–107. https://doi.org/10.1039/d0bm01247e PMID: 33325920
48. Boudou T, Legant WR, Mu A, Borochin MA, Thavandiran N, Radisic M, et al. A microfabricated platform to measure and manipulate the mechanics of engineered cardiac microtissues. Tissue Eng Part A. 2012;18(9–10):910–9. https://doi.org/10.1089/ten.tea.2011.0341 PMID: 22092279
49. Ewoldt JK, Wang MC, McLellan MA, Cloonan PE, Chopra A, Gorham J, et al. Hypertrophic cardiomyopathy-associated mutations drive stromal activation via EGFR-mediated paracrine signaling. Sci Adv. 2024;10(42):eadi6927. https://doi.org/10.1126/sciadv.adi6927 PMID: 39413182
50. Zhao Y, Rafatian N, Feric NT, Cox BJ, Aschar-Sobbi R, Wang EY, et al. A Platform for Generation of Chamber-Specific Cardiac Tissues and Disease Modeling. Cell. 2019;176(4):913–27.e18. https://doi.org/10.1016/j.cell.2018.11.042 PMID: 30686581
51. Karakan MÇ, Ewoldt JK, Segarra AJ, Sundaram S, Wang MC, White AE, et al. Geometry and length control of 3D engineered heart tissues using direct laser writing. Lab Chip. 2024;24(6):1685–701. https://doi.org/10.1039/d3lc00752a PMID: 38317604
52. Shi J, Tomasi C. Good features to track. In: 1994 Proceedings of IEEE conference on computer vision and pattern recognition. IEEE; 1994. p. 593–600.
53. Lucas BD, Kanade T. An Iterative Image Registration Technique with an Application to Stereo Vision. In: Proceedings of the 7th International Joint Conference on Artificial Intelligence - Volume 2. IJCAI'81. San Francisco (CA): Morgan Kaufmann Publishers Inc; 1981. p. 674–679.
54. Bouguet JY, et al. Pyramidal implementation of the affine lucas kanade feature tracker description of the algorithm. Intel Corporation. 2001;5(1–10):4.
55. Ronaldson-Bouchard K, Ma SP, Yeager K, Chen T, Song L, Sirabella D, et al. Advanced maturation of human cardiac tissue grown from pluripotent stem cells. Nature. 2018;556(7700):239–43. https://doi.org/10.1038/s41586-018-0016-3 PMID: 29618819
56. Dhand AP, Juarros MA, Martin TG, Garay-Sarmiento M, Alamana C, Hunt DR, et al. Digital light processing 3D printing enables versatile fabrication of human engineered heart tissues. Cell Biomaterials. 2026;:100405. https://doi.org/10.1016/j.celbio.2026.100405
57. Méry A, Ruppel A, Revilloud J, Balland M, Cappello G, Boudou T. Light-driven biological actuators to probe the rheology of 3D microtissues. Nat Commun. 2023;14(1):717. https://doi.org/10.1038/s41467-023-36371-w PMID: 36759504
58. Scalzo S, Afonso MQL, da Fonseca NJ Jr, Jesus ICG, Alves AP, Mendonça CATF, et al. Dense optical flow software to quantify cellular contractility. Cell Rep Methods. 2021;1(4):100044. https://doi.org/10.1016/j.crmeth.2021.100044 PMID: 35475144
59. Zimmerman JA, Bammann DJ, Gao H. Deformation gradients for continuum mechanical analysis of atomistic simulations. Int J Solids Struct. 2009;46(2):238–53. https://doi.org/10.1016/j.ijsolstr.2008.08.036
60. Benkley T, Li C, Kolinski J. Estimation of the Deformation Gradient Tensor by Particle Tracking Near a Free Boundary with Quantified Error. Exp Mech. 2023;63(7):1255–70. https://doi.org/10.1007/s11340-023-00981-8 PMID: 37780097
61. Virtanen P, Gommers R, Oliphant TE, Haberland M, Reddy T, Cournapeau D, et al. SciPy 1.0: fundamental algorithms for scientific computing in Python. Nat Methods. 2020;17(3):261–72. https://doi.org/10.1038/s41592-019-0686-2 PMID: 32015543
62. SciPy Developers. scipy.interpolate.RBFInterpolator — SciPy v1.13.1 Manual. 2024. Accessed on 2025-11-19. Available from: https://docs.scipy.org/doc/scipy-1.13.1/reference/generated/scipy.interpolate.RBFInterpolator.html#scipy.interpolate.RBFInterpolator
63. Pearson K. LIII. On lines and planes of closest fit to systems of points in space. Lond Edinb Dublin Philos Mag J Sci. 1901;2(11):559–72. https://doi.org/10.1080/14786440109462720
64. Hotelling H. Relations between two sets of variates. In: Breakthroughs in statistics: methodology and distribution. Springer; 1992. p. 162–90.
65. Abney TM, Feng Y, Pless R, Okamoto RJ, Genin GM, Bayly PV. Principal component analysis of dynamic relative displacement fields estimated from MR images. PLoS One. 2011;6(7):e22063. https://doi.org/10.1371/journal.pone.0022063 PMID: 21811560
66. Grama SN, Subramanian SJ. Computation of Full-field Strains Using Principal Component Analysis. Exp Mech. 2014;54(6):913–33. https://doi.org/10.1007/s11340-013-9800-z
67. Tyagi M, Wang Y, Hall TJ, Barbone PE, Oberai AA. Improving three-dimensional mechanical imaging of breast lesions with principal component analysis. Med Phys. 2017;44(8):4194–203. https://doi.org/10.1002/mp.12372 PMID: 28547868

68. Arzani A, Dawson STM. Data-driven cardiovascular flow modelling: examples and opportunities. J R Soc Interface. 2021;18(175):20200802. https://doi.org/10.1098/rsif.2020.0802 PMID: 33561376
69. Lu H, Plataniotis KNK, Venetsanopoulos AN. MPCA: Multilinear Principal Component Analysis of Tensor Objects. IEEE Trans Neural Netw. 2008;19(1):18–39. https://doi.org/10.1109/TNN.2007.901277 PMID: 18269936
70. Lu H, Plataniotis KN, Venetsanopoulos AN. A survey of multilinear subspace learning for tensor data. Pattern Recognit. 2011;44(7):1540–51. https://doi.org/10.1016/j.patcog.2011.01.004
71. Pedregosa F, Varoquaux G, Gramfort A, Michel V, Thirion B, Grisel O, et al. Scikit-learn: Machine Learning in Python. J Mach Learn Res. 2011;12:2825–30.
72. Wall ME, Rechtsteiner A, Rocha LM. Singular Value Decomposition and Principal Component Analysis. Boston (MA): Springer US; 2003. p. 91–109.
73. Lee S-J, Lee S-H. Flow field analysis of a turbulent boundary layer over a riblet surface. Exp Fluids. 2001;30(2):153–66. https://doi.org/10.1007/s003480000150
74. Adrian RJ, Christensen KT, Liu Z-C. Analysis and interpretation of instantaneous turbulent velocity fields. Exp Fluids. 2000;29(3):275–90. https://doi.org/10.1007/s003489900087
75. Helman J, Hesselink L. Representation and display of vector field topology in fluid flow data sets. Computer. 1989;22(8):27–36. https://doi.org/10.1109/2.35197
76. Helman JL, Hesselink L. Visualizing vector field topology in fluid flows. IEEE Comput Grap Appl. 1991;11(3):36–46. https://doi.org/10.1109/38.79452
77. Perry AE, Fairlie B. Critical points in flow patterns. In: Advances in geophysics. vol. 18. Elsevier; 1975. p. 299–315.
78. Perry AE, Chong MS. A Description of Eddying Motions and Flow Patterns Using Critical-Point Concepts. Annu Rev Fluid Mech. 1987;19(1):125–55. https://doi.org/10.1146/annurev.fl.19.010187.001013
79. Shu C-F, Jain RC. Vector field analysis for oriented patterns. IEEE Trans Pattern Anal Machine Intell. 1994;16(9):946–50. https://doi.org/10.1109/34.310692
80. Effenberger F, Weiskopf D. Finding and classifying critical points of 2D vector fields: a cell-oriented approach using group theory. Comput Visual Sci. 2010;13(8):377–96. https://doi.org/10.1007/s00791-011-0152-x
81. Townsend RG, Gong P. Detection and analysis of spatiotemporal patterns in brain activity. PLoS Comput Biol. 2018;14(12):e1006643. https://doi.org/10.1371/journal.pcbi.1006643 PMID: 30507937
82. Hamid AA, Frank MJ, Moore CI. Wave-like dopamine dynamics as a mechanism for spatiotemporal credit assignment. Cell. 2021;184(10):2733–49.e16. https://doi.org/10.1016/j.cell.2021.03.046 PMID: 33861952
83. Xu Y, Long X, Feng J, Gong P. Interacting spiral wave patterns underlie complex brain dynamics and are related to cognitive processing. Nat Hum Behav. 2023;7(7):1196–215. https://doi.org/10.1038/s41562-023-01626-5 PMID: 37322235
84. Qiu X, Zhang Y, Martin-Rufino JD, Weng C, Hosseinzadeh S, Yang D, et al. Mapping transcriptomic vector fields of single cells. Cell. 2022;185(4):690–711.e45. https://doi.org/10.1016/j.cell.2021.12.045 PMID: 35108499
85. Sha Y, Qiu Y, Zhou P, Nie Q. Reconstructing growth and dynamic trajectories from single-cell transcriptomics data. Nat Mach Intell. 2024;6(1):25–39. https://doi.org/10.1038/s42256-023-00763-w PMID: 38274364
86. Zhu L, Wang J. Quantifying Landscape and Flux from Single-Cell Omics: Unraveling the Physical Mechanisms of Cell Function. JACS Au. 2025;5(8):3738–57. https://doi.org/10.1021/jacsau.5c00620 PMID: 40881418
87. Pancorbo L, Ruiperez-Campillo S, Tormos A, Guill A, Cervigon R, Alberola A, et al. Vector Field Heterogeneity for the Assessment of Locally Disorganised Cardiac Electrical Propagation Wavefronts From High-Density Multielectrodes. IEEE Open J Eng Med Biol. 2023;5:32–44. https://doi.org/10.1109/OJEMB.2023.3344349 PMID: 38445238
88. Tonko JB, Ruipérez-Campillo S, Cabero-Vidal G, Cabrera-Borrego E, Roney C, Jiménez-Jáimez J, et al. Vector field heterogeneity as a novel omnipolar mapping metric for functional substrate characterization in scar-related ventricular tachycardias. Heart Rhythm. 2025;22(5):1218–28. https://doi.org/10.1016/j.hrthm.2024.10.066 PMID: 39515493
89. Theisel H, Weinkauf T, Hege H-C, Seidel H-P. Topological methods for 2D time-dependent vector fields based on stream lines and path lines. IEEE Trans Vis Comput Graph. 2005;11(4):383–94. https://doi.org/10.1109/TVCG.2005.68 PMID: 16138549
90. Liu T, Salazar DM. Two-dimensional vector field topology and scalar fields in viscous flows: Reconstruction methods. Phys Fluids. 2024;36(7). https://doi.org/10.1063/5.0215393
91. Brasselet JP, Seade J, Suwa T. Vector fields on singular varieties. vol. 1987. Springer Science & Business Media; 2009.
92. Rubner Y, Guibas LJ, Tomasi C. The earth mover's distance, multi-dimensional scaling, and color-based image retrieval. In: Proceedings of the ARPA image understanding workshop. vol. 661. 1997. 668 p.
93. Li X, Cui D, Jiruska P, Fox JE, Yao X, Jefferys JGR. Synchronization measurement of multiple neuronal populations. J Neurophysiol. 2007;98(6):3341–8. https://doi.org/10.1152/jn.00977.2007 PMID: 17913983
94. Shearme J, Leach P. Some experiments with a simple word recognition system. IEEE Trans Audio Electroacoust. 1968;16(2):256–61. https://doi.org/10.1109/tau.1968.1161985

95. Rubner Y, Tomasi C, Guibas LJ. A metric for distributions with applications to image databases. In: Sixth international conference on computer vision (IEEE Cat. No. 98CH36271). IEEE; 1998. p. 59–66.
96. Lavin Y, Batra R, Hesselink L. Feature comparisons of vector fields using earth mover's distance. In: Proceedings Visualization'98 (Cat. No. 98CB36276). IEEE; 1998. p. 103–9.
97. Rimehaug AE, Stasik AJ, Hagen E, Billeh YN, Siegle JH, Dai K, et al. Uncovering circuit mechanisms of current sinks and sources with biophysical simulations of primary visual cortex. elife. 2023;12:e87169. https://doi.org/10.7554/eLife.87169 PMID: 37486105
98. Ramdas A, Trillos N, Cuturi M. On Wasserstein Two-Sample Testing and Related Families of Nonparametric Tests. Entropy. 2017;19(2):47. https://doi.org/10.3390/e19020047
99. Lu Z. Multi-Dimensional Wasserstein Distance Implementation in Scipy. arXiv preprint arXiv:251023651. 2025. https://doi.org/10.48550/arXiv.2510.23651
100. SciPy Developers. scipy.stats.wasserstein_distance_nd — SciPy v1.13.1 Manual. 2024. Accessed on 2025-11-23. Available from: https://docs.scipy.org/doc/scipy-1.13.1/reference/generated/scipy.stats.wasserstein_distance_nd.html
101. Patel TP, Ventre SC, Meaney DF. Dynamic changes in neural circuit topology following mild mechanical injury in vitro. Ann Biomed Eng. 2012;40(1):23–36. https://doi.org/10.1007/s10439-011-0390-6 PMID: 21994056
102. Dunn OJ. Multiple Comparisons among Means. J Am Stat Assoc. 1961;56(293):52–64. https://doi.org/10.1080/01621459.1961.10482090
103. Itakura F. Minimum prediction residual principle applied to speech recognition. IEEE Trans Acoust Speech Signal Process. 1975;23(1):67–72. https://doi.org/10.1109/tassp.1975.1162641
104. Sakoe H, Chiba S. Dynamic programming algorithm optimization for spoken word recognition. IEEE Trans Acoust Speech Signal Process. 1978;26(1):43–9. https://doi.org/10.1109/tassp.1978.1163055
105. Berndt DJ, Clifford J. Using dynamic time warping to find patterns in time series. In: Proceedings of the 3rd international conference on knowledge discovery and data mining. AAAIWS'94. AAAI Press; 1994. p. 359–70.
106. Jeong Y-S, Jeong MK, Omitaomu OA. Weighted dynamic time warping for time series classification. Pattern Recognit. 2011;44(9):2231–40. https://doi.org/10.1016/j.patcog.2010.09.022
107. Olivares-Alarcos A, Foix S, Alenyà G. On Inferring Intentions in Shared Tasks for Industrial Collaborative Robots. Electronics. 2019;8(11):1306. https://doi.org/10.3390/electronics8111306
108. Miralles-Pechuán L, Kumar A, Suárez-Cetrulo AL. Forecasting COVID-19 cases using dynamic time warping and incremental machine learning methods. Exp Syst. 2023;40(6):e13237. https://doi.org/10.1111/exsy.13237
109. Meert W, Hendrickx K, Van Craenendonck T, Robberechts P, Blockeel H, Davis J. DTAIDistance. 2020. Available from: https://github.com/wannesm/dtaidistance
110. Healy J, McInnes L. Uniform manifold approximation and projection. Nat Rev Methods Primers. 2024;4(1). https://doi.org/10.1038/s43586-024-00363-x
111. van der Maaten L, Hinton G. Visualizing data using t-SNE. J Mach Learn Res. 2008;9(Nov):2579–605.
112. Jilberto J, DePalma SJ, Lo J, Kobeissi H, Quach L, Lejeune E, et al. A data-driven computational model for engineered cardiac microtissues. Acta Biomater. 2023;172:123–34. https://doi.org/10.1016/j.actbio.2023.10.025 PMID: 37879587
113. Jilberto J, DePalma SJ, Ntim D, Kobeissi H, Lejeune E, Helms A, et al. Evaluating constrained and unconstrained mixture frameworks for predicting engineered heart tissue mechanics. Acta Biomater. 2026;217:424–42. https://doi.org/10.1016/j.actbio.2026.05.007 PMID: 42119932
114. Belsley DA, Kuh E, Welsch RE. Regression diagnostics: identifying influential data and sources of collinearity. John Wiley & Sons; 2005.
115. Spearman C. The Proof and Measurement of Association between Two Things. Am J Psychol. 1904;15(1):72. https://doi.org/10.2307/1412159
116. Anscombe FJ. Graphs in Statistical Analysis. Am Stat. 1973;27(1):17–21. https://doi.org/10.1080/00031305.1973.10478966
117. Mukaka MM. Statistics corner: A guide to appropriate use of correlation coefficient in medical research. Malawi Med J. 2012;24(3):69–71. PMID: 23638278
118. Pakay J. Foundations of biomedical science: quantitative literacy: theory and problems. La Trobe eBureau; 2023.
119. Kruskal WH, Wallis WA. Use of ranks in one-criterion variance analysis. J Am Stat Assoc. 19531952;4847(264)(260):907583–621. https://doi.org/10.1080/01621459.1952.10483441
120. Dinno A. Nonparametric Pairwise Multiple Comparisons in Independent Groups using Dunn's Test. Stata J. 2015;15(1):292–300. https://doi.org/10.1177/1536867x1501500117
121. Kelley TL. An Unbiased Correlation Ratio Measure. Proc Natl Acad Sci U S A. 1935;21(9):554–9. https://doi.org/10.1073/pnas.21.9.554 PMID: 16577689
122. Field A. Discovering statistics using IBM SPSS statistics. Sage Publications Limited; 2024.
123. Dunn OJ. Multiple Comparisons Using Rank Sums. Technometrics. 1964;6(3):241–52. https://doi.org/10.1080/00401706.1964.10490181
124. Holm S. A simple sequentially rejective multiple test procedure. Scand J Stat. 1979;:65–70.

125. Simonsohn U, Nelson LD, Simmons JP. P-curve: a key to the file-drawer. J Exp Psychol Gen. 2014;143(2):534–47. https://doi.org/10.1037/a0033242 PMID: 23855496

126. Forstmeier W, Wagenmakers EJ, Parker TH. Detecting and avoiding likely false-positive findings–a practical guide. Biol Rev. 2017;92(4):1941–68. https://doi.org/10.1111/brv.12315

127. Weston SJ, Ritchie SJ, Rohrer JM, Przybylski AK. Recommendations for increasing the transparency of analysis of preexisting data sets. Adv Methods Pract Psychol Sci. 2019;2(3):214–27. https://doi.org/10.1177/2515245919848684

128. Lakens D, Mesquida C, Rasti S, Ditroilo M. The benefits of preregistration and Registered Reports. Evid-Bas Toxicol. 2024;2(1). https://doi.org/10.1080/2833373x.2024.2376046

129. Anderson MJ. Permutational Multivariate Analysis of Variance (PERMANOVA). Wiley StatsRef: Statistics Reference Online. Wiley; 2017. p. 1–15.

130. Weinfurt KP. Multivariate analysis of variance. Reading and understanding multivariate statistics. American Psychological Association; 1995. p. 245–76.

131. Rideout JR, Caporaso G, Bolyen E, McDonald D, Vázquez Baeza Y, Cañardo Alastuey J, et al. biocore/scikit-bio: scikit-bio 0.5. 9: Maintenance release. 2023. https://doi.org/10.5281/zenodo.593387

132. Rios B, Bu A, Sheehan T, Kobeissi H, Kohli S, Shah K, et al. Mechanically programming anisotropy in engineered muscle with actuating extracellular matrices. Device. 2023;1(4):100097. https://doi.org/10.1016/j.device.2023.100097